The Visual Computer (2026) 42:134
https://doi.org/10.1007/s00371-025-04341-6

RESEARCH

An adaptive hybrid metaheuristic algorithm for satellite images in remote sensing image segmentation

M. Faruk Şahin[1,2] · **Ferzat Anka**[2]

Received: 4 September 2025 / Accepted: 27 December 2025

Abstract

In recent years, the effective processing of high-resolution color satellite images obtained through remote sensing technologies has become a critical requirement in key applications such as environmental monitoring, urban planning, and disaster management. Color satellite imagery offers rich information, enabling more detailed analysis of land use, vegetation cover, and other surface characteristics. In this context, multi-level image thresholding techniques are widely employed to enhance segmentation quality; however, achieving both high accuracy and low computational cost in complex scenes remains a significant challenge. To address these challenges, this study proposes the RSA-HGSO algorithm, an adaptive hybrid structure that combines the Reptile Search Algorithm (RSA) and Henry Gas Solubility Optimization (HGSO). By integrating RSA's global exploration capabilities with HGSO's local exploitation strengths, RSA-HGSO ensures both solution diversity and fast, stable convergence. Experimental analyses conducted on high-resolution color satellite images from the NASA Visible Earth dataset demonstrate the algorithm's efficient performance. With average values of PSNR = 24.59 dB, SSIM = 0.9088, FSIM = 0.9233, and NCC = 0.9663, RSA–HGSO outperforms comparative methods in terms of both accuracy and structural integrity. Furthermore, correlation analyses indicate that the original pixel intensity ranking is preserved at a rate of 91% after segmentation (Pearson = 0.9557, Spearman = 0.9549), and neighborhood relationships are largely maintained (Pearson = 0.8042, Spearman = 0.8051). Ablation studies further confirm that RSA–HGSO not only integrates the performance of its component algorithms but also complements exploration and exploitation processes in a synergistic manner, resulting in more balanced and robust outcomes. The findings suggest that the RSA–HGSO algorithm offers a balanced, scalable, and computationally efficient solution to the problem of color multi-level satellite image thresholding and presents a practical method applicable to real-world tasks such as disaster management, agricultural monitoring, and urban planning.

Keywords Hybrid meta-heuristics · Computer vision · Multi-level image thresholding · Remote sensing · Satellite image segmentation

1 Introduction

In recent years, remote sensing technologies have been widely employed for the analysis of images acquired from satellites or aerial platforms to obtain information about the Earth and the atmosphere [1–3]. Consequently, they play a critical role in various domains, including environmental monitoring [4], agricultural yield analysis [5], urban planning [6], disaster management [7], and the sustainable management of natural resources [8] among others [9–11]. Most of these images are provided in color (RGB) format, combining red, green, and blue bands to deliver a natural color appearance, thereby offering information interpretable by the human eye [12]. However, the high information density in such images makes the accurate separation of different objects and regions a challenging task [13]. Accurate segmentation is of critical importance for obtaining reliable and meaningful results in applications such as land cover detection, urban area analysis, classification of agricultural fields, and the assessment of the impacts of natural disasters such as floods, landslides, and wildfires [14–16]. Nevertheless, single-level thresholding or manual threshold determination methods often lead to loss of detail, misclassification, and low

✉ M. Faruk Şahin
Muhammed.sahin@atlas.edu.tr

[1] Department of Computer Engineering, Istanbul Atlas University, Istanbul, Turkey

[2] Data Science Application and Research Center (VEBIM), Fatih Sultan Mehmet Vakif University, Istanbul, Turkey

Published online: 21 January 2026

accuracy in complex scenes [17]. In this context, multi-level image thresholding techniques provide a means of partitioning an image into specific brightness ranges, thereby enabling clearer identification of target regions.

Classical thresholding methods such as Otsu's between-class variance maximization and Kapur's entropy criterion are widely used because they are conceptually simple and effective on moderate-complexity images [18]. However, their computational burden grows rapidly with the number of thresholds, and their performance can degrade in the presence of noise, spectral overlap, or multimodal distributions typical of high-resolution remote sensing data [19]. These limitations are particularly evident for color imagery, where inter-channel dependencies and non-Gaussian class statistics violate assumptions implicit in many analytic formulations and necessitate joint optimization of per-channel thresholds. As a result, purely analytical schemes may produce sub-optimal partitions or require prohibitive search, motivating data-driven optimization strategies tailored to RGB scenes.

To address these challenges, Meta-Heuristic (MH) optimization algorithms have gained increasing attention in recent years [20, 21]. MH algorithms offer significant advantages, including the ability to locate solutions close to the global optimum within a large search space, adaptability to diverse problem types, flexibility in parameter tuning, and robustness in avoiding local minima [22, 23]. In the case of color remote sensing images, these algorithms can automatically optimize threshold values for each color channel, thereby improving segmentation quality and enabling more efficient delineation of object boundaries [24, 25]. As a result, they substantially enhance computational efficiency and reduce processing time. Additional benefits include more effective modeling of complex color distributions, mitigation of illumination variations, and improved exploitation of spectral features. Nevertheless, studies in the literature applying MH algorithms to the multi-level thresholding problem of color images remain limited, with most research focusing primarily on grayscale imagery [26]. This situation leads to a loss of spectral information through color-space transformation while increasing the risk of premature convergence within the high-dimensional search space of high-level thresholding problems. Due to the unique noise characteristics, complexity, and large data volume of satellite imagery, these limitations necessitate the development of novel and well-balanced search strategies. Multi-level segmentation of satellite imagery extends beyond a theoretical optimization problem, possessing direct application potential in critical domains such as disaster management, agricultural yield estimation, urban growth monitoring, and the sustainable management of natural resources. For instance, in the case of sudden natural disasters such as floods and wildfires, rapid segmentation enables the automatic identification of affected areas, while in agricultural regions, it facilitates the accurate classification of crop types for productivity analysis. Similarly, in urban planning processes, the precise classification of buildings, roads, and green spaces is of significant importance for decision-support systems. In this context, the efficient performance demonstrated by the proposed hybrid algorithm particularly at low and intermediate threshold levels has practical qualities that can be directly transferred to real-world field applications.

1.1 Motivation and contribution

The primary motivation of this study is to develop a computationally efficient and highly accurate method for the multi-level thresholding of color remote sensing images. Although numerous MH-based optimization approaches have been reported for grayscale images, similar studies targeting RGB-format remote sensing imagery are scarce. To bridge this gap, a novel adaptive hybrid optimization framework is proposed. In this approach, the Reptile Search Algorithm (RSA) and the Henry Gas Solubility Optimization (HGSO) algorithm are integrated into a hybrid structure. The RSA demonstrates strong exploration ability to effectively scan a wide solution space, whereas HGSO provides powerful exploitation capability for achieving high-quality local solutions. By adaptively combining these two algorithms, the proposed method enhances both solution diversity and convergence speed. In addition, although hybrid models such as PSO–GWO and GWO–WOA have been proposed in the literature, these studies generally overlook the multi-channel dependencies present in color (RGB) satellite imagery. Moreover, existing hybrid approaches typically execute the exploration and exploitation phases sequentially, which tends to increase the risk of premature convergence and computational overhead, especially when dealing with a high number of thresholds. In contrast to this conventional sequential framework, the proposed RSA–HGSO method adaptively distributes exploration and exploitation processes in a dynamic manner. As a result, the strong global search capability of RSA is effectively balanced with the high-quality local search mechanism of HGSO, enabling efficient performance in terms of both accuracy and computational cost—particularly on high-resolution color satellite images. In this respect, the proposed approach presents a novel framework that overcomes the limitations of existing hybrid methods.

The main contributions of this study can be summarized as follows:

- A novel hybrid RSA-HGSO algorithm is designed for the multi-level thresholding of color remote sensing images. This framework dynamically integrates the broad search capability of RSA with the precise convergence strength of HGSO.

- By combining the strengths of RSA and HGSO, the proposed method achieves a balanced execution of exploration and exploitation phases.
- The method is evaluated on high-resolution images obtained from the NASA Visible Earth platform and compared with existing approaches in terms of both visual quality and quantitative metrics.
- The experimental results demonstrate that the proposed algorithm delivers high accuracy, fast convergence, and low computational cost, confirming its efficiency for multilevel color image thresholding.

The remainder of this paper is organized as follows: Sect. 2 reviews related work. Section 3 details the proposed method's framework. Section 4 presents experimental results. Sections 5 and 6 discuss the findings and the strongest side of the study and its limitations. Finally, Sect. 7 concludes the paper by summarizing key outcomes and highlighting potential directions for future research.

2 Related works

In this section, the existing literature on remote sensing image thresholding techniques is comprehensively reviewed, and relevant methods are categorized under their respective subtopics. This provides a clear overview of the current state of research in the problem domain addressed in this study, as well as the fundamental characteristics of the techniques employed.

2.1 Image thresholding techniques in remote sensing

Among the widely used thresholding approaches, Tsallis entropy has shown limitations in multi-level segmentation tasks due to its unextended parameter "q." To address this issue, an adaptive Tsallis entropy algorithm has been proposed by examining the relationship between the "q" parameter and the long-range correlations of pixels for multi-thresholding applications [27]. This method has been applied to infrared, medical CT, and color satellite imagery, demonstrating superior performance in terms of Peak Signal-to-Noise Ratio (PSNR) and Structural Similarity Index Measure (SSIM) when compared with Shannon entropy and classical Tsallis algorithms. Moreover, for similar scenes, the "q" parameter can be constrained to a narrow range while maintaining long-range correlations. In another study, conventional wavelet transforms were found to be insufficient for preserving edge details in remote sensing images due to pseudo-Gibbs effects and blurring. To overcome this limitation, an optimized contourlet transform combined with an eight-direction filter bank was employed to decompose images into directional components and better capture features [28]. Using a semi-soft thresholding function to process the transformed coefficients, the method achieved more efficient edge reconstruction. Simulation results indicated improvements in PSNR values and noise suppression by approximately 0.11% compared to traditional wavelet- and contourlet-based thresholding methods. The accurate detection of water bodies from satellite imagery is crucial for maintaining ecological balance. However, due to the significant speckle noise present in SAR imagery, conventional filtering-based methods often lose important details. To address this problem, a self-adaptive thresholding method was proposed, wherein images were divided into uniform blocks using orbit-dependent distance layers, followed by Otsu thresholding and the Jeffries-Matusita distance [29]. While the global Otsu method achieved only 93.8% overall accuracy (OA), the optimized method improved OA by at least 3.2% and the Kappa coefficient by 5.1%. Nevertheless, distinguishing water from non-water pixels in complex backgrounds remained challenging. To address this, an automatic surface water detection framework that optimizes Otsu thresholds was introduced [30]. Evaluated on Landsat-9 imagery, the approach achieved OA above 99%, a Kappa coefficient in the range of 0.961–0.998, and F1-scores between 0.977–0.998. Thus, the method effectively mitigated the shortcomings of Tsallis and SAR-based techniques, automatically selecting the most suitable water index across different scenes and yielding more robust results for time-series analysis. However, its accuracy was still limited in non-water classes or under complex land surface conditions. In another line of research, the identification of shallow landslide areas in low-resolution remote sensing imagery has been hindered by complex illumination conditions and spectral similarities. To mitigate this challenge, the application of Retinex theory was proposed [31]. By incorporating multi-scale features, morphological opening and closing transformations, and sliding-window computations, segmentation was performed using Otsu thresholding. Experimental results demonstrated a recognition rate exceeding 95% for shallow landslide regions. However, as the method was optimized specifically for shallow landslide detection, it could not be generalized to water or other land-cover classes, and its performance was limited in SAR images with severe speckle noise or low contrast. To further address the intra-class dissimilarity and inter-class similarity problem in remote sensing segmentation, a deep learning-based semantic segmentation framework was proposed [32]. The model employed a Multipath Fusion Module (MFM) to extract features from input images and dynamically merged features from multiple paths. During fusion, the model adaptively adjusted the contribution of each path and the feature threshold according to the input image, thereby

enhancing segmentation accuracy. In the upsampling stage, a guided strategy was used to mitigate edge misclassification caused by bilinear interpolation. Experiments on the Potsdam dataset reported mean Intersection over Union (mIoU) of 83.38%, overall accuracy (OA) of 90.21%, and an F1-score of 90.86%. Despite these promising results, the proposed method requires a large amount of labeled training data, thereby limiting its applicability in scenarios with scarce annotations.

Traditional semantic segmentation algorithms face limitations in landslide detection due to the diverse shapes and textures of landslides, the abundance of spectral features, and the complexity of the surrounding environment in remote sensing imagery, often resulting in misclassifications. To address this, a novel model specifically designed for accurate landslide segmentation in high-resolution optical remote sensing imagery, termed LandslideNet, has been proposed [33]. The proposed method introduces several architectural enhancements to the YOLOv8 backbone. First, a Lightweight Spatial Adaptive Weight Convolution (LSAWC) module is integrated to improve the model's local feature extraction capability, thereby enhancing its ability to detect small-scale landslides. Second, to adapt to the complex geometries of landslides, a convolutional block termed Adaptive-Deformable Convnets (Adaptive-DCN), based on a Compound Weight Attention (CWA) mechanism, is incorporated into the backbone to more effectively extract landslide-specific features. Third, to improve the extraction of features from landslides with large aspect ratios, Dynamic Snake Convolution (DSConv) is added to the backbone. Finally, a Diverse Branch Block (DBB) is integrated into the neck of YOLOv8 to enhance feature fusion capability. Quantitative experimental results demonstrate that LandslideNet outperforms widely used semantic segmentation models, including U-Net, PSPNet, Deeplabv3 + , HRNetv2, Segformer, and GELAN-c, achieving F1-score, mIoU, FWIoU, mPA, and OA values of 72.53%, 78.41%, 99.86%, 83.33%, and 99.93%, respectively. However, the model exhibits disadvantages in terms of generalization ability, computational complexity, and high processing cost. Hyperspectral data used in satellite imaging also present challenges due to high dimensionality, significant spectral redundancy, and inherent noise, leading to increased computational complexity in both spatial and temporal domains. To address this, a fusion of Mutual Information (MI) and the Otsu thresholding method has been proposed [34]. The method employs three different entropy measures—joint, conditional, and relative—to guide hyperspectral band selection. Probabilities, entropy, and mutual information between hyperspectral bands are first computed, and the optimal threshold is determined using Otsu multi-thresholding to select the most informative bands. Furthermore, Support Vector Machine (SVM) classification is applied to improve classification efficiency with the selected bands. Experimental analysis on the Indian Pines dataset shows that the relative method achieves superior accuracy (92.16%) compared to joint and conditional methods. While the method delivers competitive performance with fewer selected bands, further evaluation through nonlinear spectral unmixing is required. Due to the randomness and confidentiality of solid waste disposal sites, manual field inspections and visual interpretation of remote sensing imagery are costly in terms of time and labor. To address this challenge, a network architecture termed Two-Step Detection Network (TSNET) has been proposed [35]. In the first detection stage, a segmentation model named Segmentation with Feature Enhancement-YOLO (SFE-YOLO) is designed to separate waste categories. In the second detection stage, waste identified in the first stage is further classified into construction, domestic, and mixed waste using a ResNet architecture. Experimental results on five waste categories show that the method achieves a mean Average Precision (mAP) of 84.1% and an Average Precision (AP) of 79.0%, outperforming conventional approaches. Nonetheless, the method suffers from computational and time costs. In the domain of building footprint extraction from satellite imagery, challenges remain due to the complex structures, varying scales, and diverse appearances of buildings. To address difficulties in detecting small buildings and mitigating segmentation errors along edges, the Multiple Attending Path Neural Network (MAP-Net) has been introduced [36]. The method progressively constructs multiple parallel paths to learn high-level semantic features while preserving spatial localization. An attention module adaptively compresses channel-wise features extracted from each path for optimized multi-scale fusion, while a pyramid spatial pooling module captures global dependencies to refine fragmented building footprints. Experimental results on the Urban 3-D, Deep Globe, and WHU datasets show improvements over the state-of-the-art HRNetv2, achieving F1-score increases of 0.88%, 0.93%, and 0.45%, and IoU score gains of 1.53%, 1.50, and 0.82%, respectively. However, the method is constrained by its inability to identify land cover and similar non-building classes.

2.2 Meta heuristics in multi-level image thresholding segmentation for remote sensing

Satellite image segmentation is one of the most challenging tasks, as it must account for complete randomness, multiple regions of interest, weak pixel correlations, and uncertain boundary areas. To address these challenges, nature-inspired algorithms have been employed to obtain the most optimal threshold values for segmentation, often yielding higher efficiency compared to traditional methods. However, their primary disadvantages lie in computational expenses and time consumption. To overcome these issues and achieve

more efficient satellite image segmentation, an adaptive Cuckoo Search Optimization (CSO) algorithm has been proposed [37]. The method incorporates two distinct objective functions, namely Otsu's method and the Tsallis entropy function, thereby improving performance in terms of PSNR, MSE, FSIM, SSIM, UIQI metrics, and computational time. Nonetheless, a limitation arises from degradation in segmentation quality at higher threshold levels. To mitigate this problem, the Coronavirus Optimization Algorithm (COVIDOA) was introduced [38]. In this approach, the concept of chaotic mapping is integrated into the initialization phase of the algorithm to enhance solution diversity. Moreover, a novel fitness function is constructed by combining Otsu's and Kapur's entropy, enabling the determination of optimal threshold values. Comparative experiments with other recent MH algorithms demonstrated improved performance. However, a major limitation is the lack of testing on color images for multi-level image thresholding. To address this gap, the Improved Bald Eagle Search algorithm (IBES) was proposed for color satellite image segmentation [39]. The method utilizes Rényi entropy to identify optimal threshold values for multi-level thresholding. To enhance the diversity of the eagle population's search domain, chaotic tent mapping and Lévy flight strategies are incorporated. As a result, the method achieves superior segmentation performance, with an SSIM value of 93%, compared to traditional techniques. Nevertheless, the absence of hyperparameter tuning presents a notable limitation. To overcome this and to improve performance in densely populated Land-Use/Land-Cover (LULC) change detection problems, the Non-dominated Sorting Genetic Algorithm (NSGA) has been applied to multispectral and very-high-resolution images [40]. The method maintains a variable-length property throughout the optimization process, leading to enhanced overall accuracy of 98.47% compared to conventional approaches. Another technique proposed for change detection is the Particle Swarm Optimization (PSO) algorithm [41], which has shown greater efficiency relative to conventional Sobel, Canny, and Prewitt edge-based methods. In a separate study, image fusion was employed in multi-spectral images to transfer the maximum possible information from source images to the fused image. A two-stage K-medoids segmentation and Differential Search Algorithm (DSA) were proposed for this purpose [42]. In this method, the fused image is generated by combining the red, green, and blue (RGB) bands of the same region using the intensity–hue–saturation (IHS) transformation, resulting in improved performance over traditional methods. Remote sensing images also present significant challenges due to the large amount of noise introduced by solar radiation, atmospheric windows, radiation deviations, and environmental effects of the sky. To address this, a parallel Sine Cosine Algorithm based on the Taguchi method (TPSCA) has been proposed to optimize parameter settings in pulse-coupled neural networks (PCNN) [43]. The Taguchi method is used to adapt the algorithm to the target problem within a parallel architecture. This approach improves segmentation accuracy, achieving 88.25% accuracy. Nonetheless, these approaches remain disadvantaged by their time and computational cost. Similarly, Otsu-based methods, although maximizing inter-class variance for segmentation, are limited by high computational expense. To address this, a Modified Snake Optimizer (MSO) algorithm has been introduced, capable of dynamically and efficiently adjusting the parameters of the Snake Optimizer (SO) [44]. Experimental results show that MSO consistently outperforms the traditional SO in benchmark functions, and that MSO-Otsu achieves superior segmentation results and faster convergence. Finally, to avoid premature convergence and improve search capability, a novel segmentation approach based on Dynamic Harris Hawks Optimization with Mutation Mechanism (DHHO/M) has been proposed [45]. Experimental validation using Kapur, Tsallis entropy, and Otsu-based criteria demonstrates enhanced efficiency over existing methods.

3 Methodology

In this study, a novel MH algorithm is proposed for performing multi-level thresholding on color satellite images, by adaptively hybridizing the Reptile Search Algorithm (RSA) with the Henry Gas Solubility Optimization (HGSO) algorithm. The RSA algorithm is particularly effective in maintaining solution diversity in high-dimensional histogram-based color image segmentation. On the other hand, HGSO provides an advantage in convergence to local optima by allowing the optimization of candidate solutions through small steps. Therefore, the combination of these two algorithms offers both diversity and precision in addressing multi-level thresholding problems in satellite imagery. In the proposed framework, the RSA algorithm is predominantly employed during the initial iterations to emphasize exploration, while the HGSO algorithm is activated in the later iterations to enhance exploitation. This adaptive structure enables the algorithm to converge more rapidly toward the global optimum while simultaneously increasing its capacity to avoid local minima. In this section, the objective function, hybrid methodology, and time complexity of the proposed approach are described in detail. The graphical abstract is presented in Fig. 1.

3.1 Objective function definition

In this study, the objective function for multi-level thresholding of color satellite images is based on a hybridization

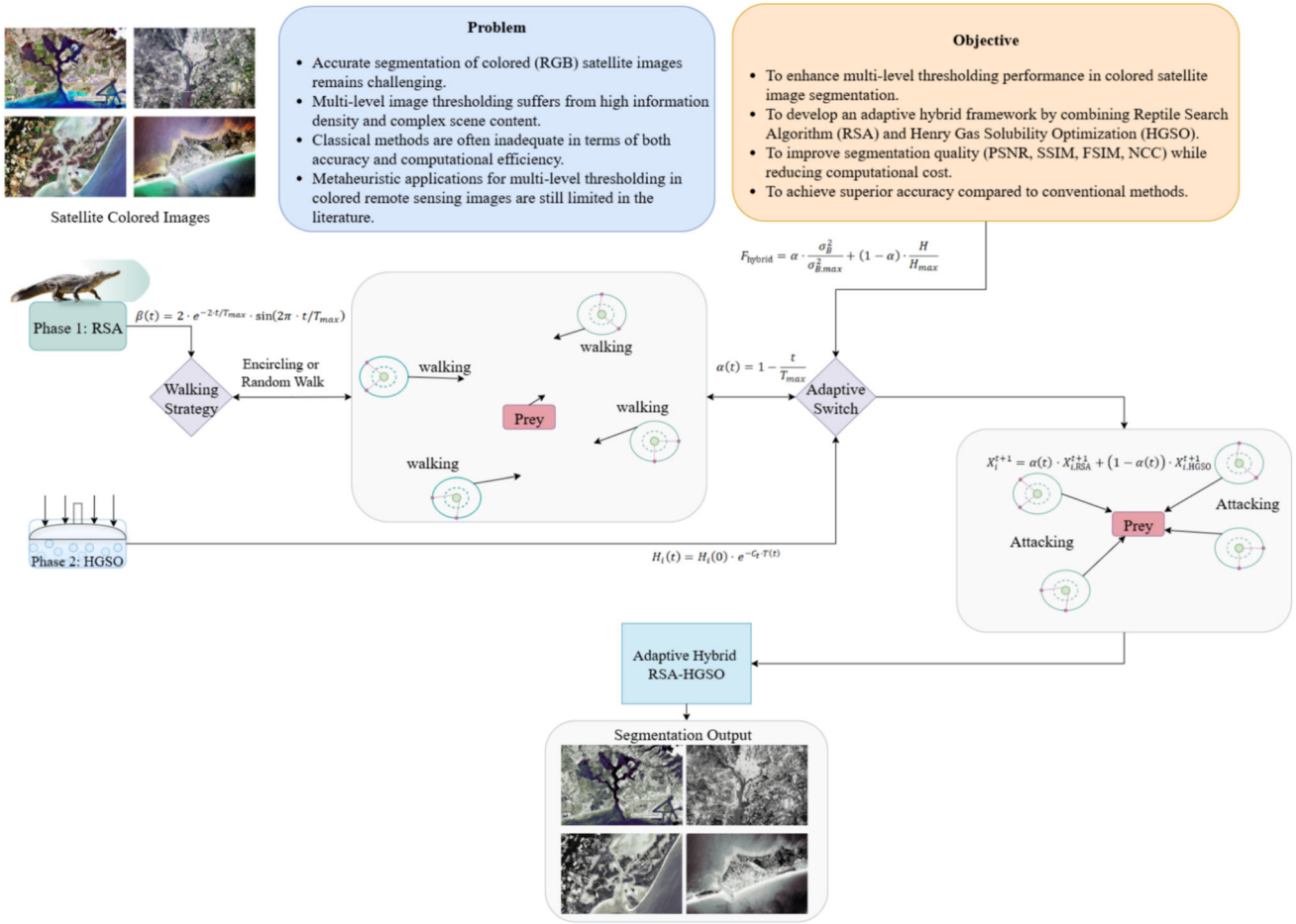

Fig. 1 Graphical abstract of proposed method

of two widely used approaches: Otsu's variance maximization method and Kapur's entropy-based method [38]. Otsu's method determines the optimal threshold values by maximizing the between-class variance σ_B^2 of the image histogram. For multi-level thresholding, m threshold values $\{t_1, t_2, \ldots, t_m\}$ partition the image into $m+1$ classes. The between-class variance is expressed in Eq. (1).

$$\sigma_B^2 = \sum_{i=1}^{m+1} \omega_i (\mu_i - \mu_T)^2 \tag{1}$$

Here, ω_i denotes the probability of pixels belonging to the i-th class, μ_i represents the mean gray level of the $i-th$ class, and μ_T is the global mean gray level of all image pixels. The objective function of Otsu's method is therefore defined as maximizing the between-class variance, i.e., $\max_{\{t_1,\ldots,t_m\}} \sigma_B^2$. Kapur's method, on the other hand, employs the concept of entropy to measure the information content of each class. For multi-level thresholding, the total entropy H is defined in Eq. (2).

$$H = \sum_{i=1}^{m+1} H_i = -\sum_{i=1}^{m+1} \sum_{j \in C_i} \frac{p_j}{\omega_i} \log\left(\frac{p_j}{\omega_i}\right) \tag{2}$$

In this equation, p_j denotes the normalized histogram value of gray level j, while ω_i represents the probability of the $i-th$ class. C_i corresponds to the gray-level range of the $i-th$ class, and N denotes the total number of pixels. The objective function of Kapur's method is defined as maximizing the total entropy, i.e., $\max_{\{t_1,\ldots,t_m\}} H$. To leverage the complementary strengths of Otsu's and Kapur's methods, a hybrid objective function is designed. While Otsu's method statistically maximizes between-class separability, Kapur's method maximizes information content. The hybrid formulation integrates the normalized scores of both methods using a weighting coefficient α, as expressed in Eq. (3).

$$F_{\text{hybrid}} = \alpha \cdot \frac{\sigma_B^2}{\sigma_{B,max}^2} + (1-\alpha) \cdot \frac{H}{H_{max}} \tag{3}$$

Here, $\left(\sigma^2_{B,max}\right)$ represents the maximum between-class variance obtained by Otsu's method, while (H_{max}) denotes the maximum entropy obtained by Kapur's method. The parameterα, ranging between $0 \leq \alpha \leq 1$, serves as a weighting factor to balance Otsu's and Kapur's contributions. Consequently, the optimization process simultaneously maximizes both between-class separability and information content. However, the proposed RSA–HGSO algorithm operates on a one-dimensional histogram by initially converting the color satellite image to grayscale $I \rightarrow I_g$ in order to compute the hybrid objective function based on Otsu's Between-Class Variance σ^2_B and Kapur's Entropy$H$. This approach is adopted as a computational trade-off to avoid a substantial increase in computational complexity at high threshold levels$T_N \approx 26$. To preserve exploration and exploitation efficiency, the algorithm employs one-dimensional (luminance) histogram–based optimization, which forms the mathematical foundation of traditional methods such as Otsu and Kapur.

3.2 Proposed RSA-HGSO methodology

In this study, the Reptile Search Algorithm (RSA) and the Henry Gas Solubility Optimization (HGSO) algorithm are adaptively hybridized to address the optimization of the multi-level thresholding problem. The RSA algorithm, inspired by the hunting behavior of reptiles, provides a strong exploration capability, particularly effective in high-dimensional search spaces. On the other hand, the HGSO algorithm, inspired by the principles of gas solubility, offers a powerful local search mechanism during the exploitation phase. In RSA, the exploration stage aims to distribute candidate solutions widely across the search space in order to identify promising regions near the global optimum. At this stage, two main strategies are mathematically modeled to simulate reptiles' surveillance and hiding behaviors. The first strategy, called High Walking, updates candidate solutions by performing a random walk around the current best solution. This process is formulated in Eq. (4).

$$X_i^{t+1} = X_{\text{best}}^t + r_1 \cdot \left(X_{\text{best}}^t - 2r_2 X_i^t\right) \tag{4}$$

Here X_i^t represents the position of the $i-th$ candidate solution at iteration t, X_{best}^t denotes the best solution found so far, and r_1, $r_2 \in [0,1]$ are random numbers. This strategy models reptiles' observation and approach behavior, dispersing candidate solutions across a wide region of the search space and supporting the discovery of the global optimum. The second strategy, referred to as Belly Walking, updates candidate solutions based on a linear combination of two randomly selected solutions from the population. This process is expressed in Eq. (5).

$$X_i^{t+1} = X_{r_1}^t + r_3 \cdot \left(X_{r_2}^t - X_i^t\right) \tag{5}$$

In this formulation, $X_{r_1}^t$ and $X_{r_2}^t$ denote two randomly chosen solutions from the population, while $r_3 \in [0,1]$ is a random number. This strategy generates new candidate solutions by combining existing ones, thereby enhancing the diversity of the population within the search space. In both strategies, the step size of the search is controlled by an adaptive coefficient that varies with the iteration number. This coefficient is defined in Eq. (6).

$$\beta(t) = 2 \cdot e^{-2 \cdot t/T_{max}} \cdot \sin(2\pi \cdot t/T_{max}) \tag{6}$$

Here, $\beta(t)$ enhances global exploration in the early iterations by taking larger steps, while in later iterations it facilitates convergence toward local optima through smaller step sizes. The HGSO algorithm, inspired by Henry's Law that defines the solubility of gases in liquids, is a MH optimization method. According to Henry's Law, the solubility of a gas in a liquid is directly proportional to its partial pressure. In HGSO, this principle is adapted to optimization by modeling candidate solutions (particles) in the search space based on concepts of pressure, temperature, and solubility. HGSO provides a strong local search capability, particularly in the exploitation phase. First, the solubility coefficient H_i for each candidate solution is updated during iterations using the temperature and Henry's constant. This update process is given in Eq. (7).

$$H_i(t) = H_i(0) \cdot e^{-C_t \cdot T(t)} \tag{7}$$

Here, $H_i(0)$ denotes the initial solubility coefficient, C_t represents the temperature variation coefficient, and $T(t)$ denotes the temperature value at iteration t. This equation ensures that the solubility coefficient decreases as iterations progress, thereby reducing the step size of candidate solutions. Subsequently, the position of each candidate solution is updated interactively with other solutions in the population, based on gas concentration. This update is expressed in Eq. (8).

$$X_i^{t+1} = X_i^t + r \cdot H_i(t) \cdot \left(X_{\text{best}}^t - X_i^t\right) \tag{8}$$

Here, $r \in [0,1]$ denotes a random number, while X_{best}^t represents the current best solution. This step ensures that candidates with higher solubility coefficients converge faster toward the optimal solution. The adaptive transition between RSA and HGSO is modeled as a function of the iteration number, as shown in Eq. (9).

$$\alpha(t) = 1 - \frac{t}{T_{max}} \tag{9}$$

Here, t denotes the current iteration, T_{max} is the maximum number of iterations, and $\alpha(t)$ represents the exploration weighting factor. At the beginning, since $\alpha(t) \approx 1$, the

exploration steps of RSA dominate. As iterations progress, $\alpha(t) \rightarrow 0$, and the exploitation steps of HGSO become dominant. The coefficient $\alpha(t)$ defined in Eq. (9) constitutes a time-dependent mechanism that depends solely on the iteration count t, independent of the algorithm's current search state. This mechanism divides the search process into two principal phases and aims to systematically adapt the global exploration (RSA) and local exploitation (HGSO) capabilities to the evolutionary process. Owing to this deterministic structure, the strong global exploratory capacity of RSA becomes dominant during the initial iterations $\alpha(t) \approx 1$, whereas the precise local exploitation and convergence behavior of HGSO emerges in the later stages $\alpha(t) \rightarrow 0$. Rather than enforcing sequential phase transitions between exploration and exploitation, this approach provides a balanced and gradual search strategy by dynamically weighting the simultaneously computed RSA and HGSO position updates (Eq. 10) through this coefficient. In this way, the algorithm is designed to leverage the strengths of both major phases in a controlled manner throughout the optimization process. Accordingly, the position update in the adaptive hybrid structure is defined in Eq. (10).

$$X_i^{t+1} = \alpha(t) \cdot X_{i,\mathrm{RSA}}^{t+1} + (1 - \alpha(t)) \cdot X_{i,\mathrm{HGSO}}^{t+1} \tag{10}$$

Here, $X_{i,\mathrm{RSA}}^{t+1}$ denotes the updated position obtained from the RSA exploration phase, while $X_{i,\mathrm{HGSO}}^{t+1}$ represents the updated position obtained from the HGSO exploitation phase. The optimal threshold vector obtained through these operations is used to generate a segmentation map that preserves the spectral information of the original color satellite image. Although the optimization is derived from a one-dimensional grayscale histogram, during segmentation, the pixels assigned to each segment are mapped back to the mean intensity values of the original color channels (RGB). In this way, the resulting output retains macrostructural features while preserving the color information. In this way, the algorithm performs wide exploration during the early stages of iterations and more refined, high-precision improvements in the later stages. The advantages of this hybrid structure can be summarized as follows.

1. The random combination and encircling prey modes of RSA enable an effective exploration of the regions where the global optimum is likely to be located.
2. Through the solubility-based convergence mechanism of HGSO, the solutions within these regions are refined with high accuracy.
3. By means of the adaptive transition coefficient $\alpha(t)$, the strengths of both algorithms are activated at the appropriate stages of the optimization process.

3.3 Complexity analysis and pseudo-code representation of the proposed method

The computational complexity of the proposed adaptive hybrid RSA–HGSO algorithm arises from the combined costs of both algorithms. Here, N denotes the population size, D represents the problem dimension, and T_{max} is the maximum number of iterations. In the RSA algorithm, each iteration requires all individuals in the population to undergo two main modes: Best-guided Random Walk and Random Combination. Since the computational cost of each mode is $O(D)$, the cost per iteration for the entire population is $O(N \cdot D)$, leading to a total complexity of $O(N \cdot D \cdot T_{max})$. In the HGSO algorithm, for each individual, the computation of the solubility coefficient, pressure values, and position updates also requires $O(D)$. Therefore, the total computational cost is similarly expressed as $O(N \cdot D \cdot T_{max})$. In the proposed hybrid structure, at each iteration both RSA and HGSO updates are performed and combined through the adaptive coefficient $\alpha(t)$. The computation of this coefficient has a cost of $O(1)$, which can be neglected. Consequently, the overall time complexity can be expressed as $O_{\mathrm{Hybrid}} = O_{\mathrm{RSA,total}} + O_{\mathrm{HGSO,total}} = O(2 \cdot N \cdot D \cdot T_{max})$, and by ignoring constant factors in asymptotic analysis, it reduces to $O(N \cdot D \cdot T_{max})$.The memory complexity arises from storing the positions of all individuals in the population $O(N \cdot D)$ and maintaining their fitness values ($O(N)$). By neglecting temporary variables, the total memory cost becomes ($O(N \cdot D)$). In conclusion, the proposed adaptive hybrid RSA–HGSO algorithm exhibits linear scalability in both time and memory complexities, which significantly enhances its applicability to high-dimensional ($D \gg 1$) and large-population ($N \gg 1$) optimization problems. The pseudo-code outlining the general operational steps of the proposed algorithm is provided in Algorithm 1, and the corresponding flowchart is illustrated in Fig. 2.

Algorithm 1: Hybrid Adaptive RSA–HGSO for Multi-level Color Satellite Image Thresholding

Input: Color satellite image I, number of thresholds T_n, weight α (Otsu–Kapur), population size N, max iterations E, switch ratio r

Output: Optimal thresholds θ^*, segmented image I_s

Step 1: Preprocessing

Convert I to grayscale I_g

Compute histogram h and probability histogram p_h of I_g

Step 2: Define Hybrid Objective Function

foreach *candidate threshold set* $\Theta = \{\theta_1, \ldots, \theta_{T_n}\}$ **do**

- Compute Otsu variance $O(\Theta)$
- Compute Kapur entropy $K(\Theta)$
- Hybrid score $H(\Theta) = \alpha \cdot O(\Theta) + (1 - \alpha) \cdot K(\Theta)$
- Fitness $f(\Theta) = -H(\Theta)$

Step 3: Initialize Parameters

Set $E_{RSA} = \lfloor r \cdot E \rfloor$, $E_{HGSO} = E - E_{RSA}$

Initialize population P of N solutions within $[1, 255]^{T_n}$

Evaluate $f(\cdot)$ for each solution

Step 4: RSA Phase (Exploration)

for $iter = 1$ **to** E_{RSA} **do**

- Compute $\beta = 2e^{-2 \cdot iter / E_{RSA}} \cdot \sin\left(\frac{2\pi \cdot iter}{E_{RSA}}\right)$
- **foreach** *solution* x_i *in* P **do**
  - With probability 0.6: ; `// Exploration`
    - Perform encircling or random walk update
  - Else: ; `// Exploitation`
    - Apply Hunting mode 1 or 2 using β
  - Apply boundary correction to x_i
  - Evaluate $f(x_i)$
- Update P and best solution x^*

Step 5: HGSO Phase (Exploitation)

Initialize HGSO population using x^* as first solution

for $iter = 1$ **to** E_{HGSO} **do**

- Update Henry's coefficient and solubility constants
- Update positions using HGSO movement rules
- Apply boundary correction and evaluate $f(\cdot)$
- Update global best x^* if better

Step 6: Return Result

$\theta^* \leftarrow \text{sort}(x^*)$

foreach *color channel* c *in RGB* **do**

- Apply multi-level thresholding with θ^* to channel c
- Replace pixels in channel c with average intensity of each segment

Combine segmented channels into final color image I_s

return θ^*, I_s

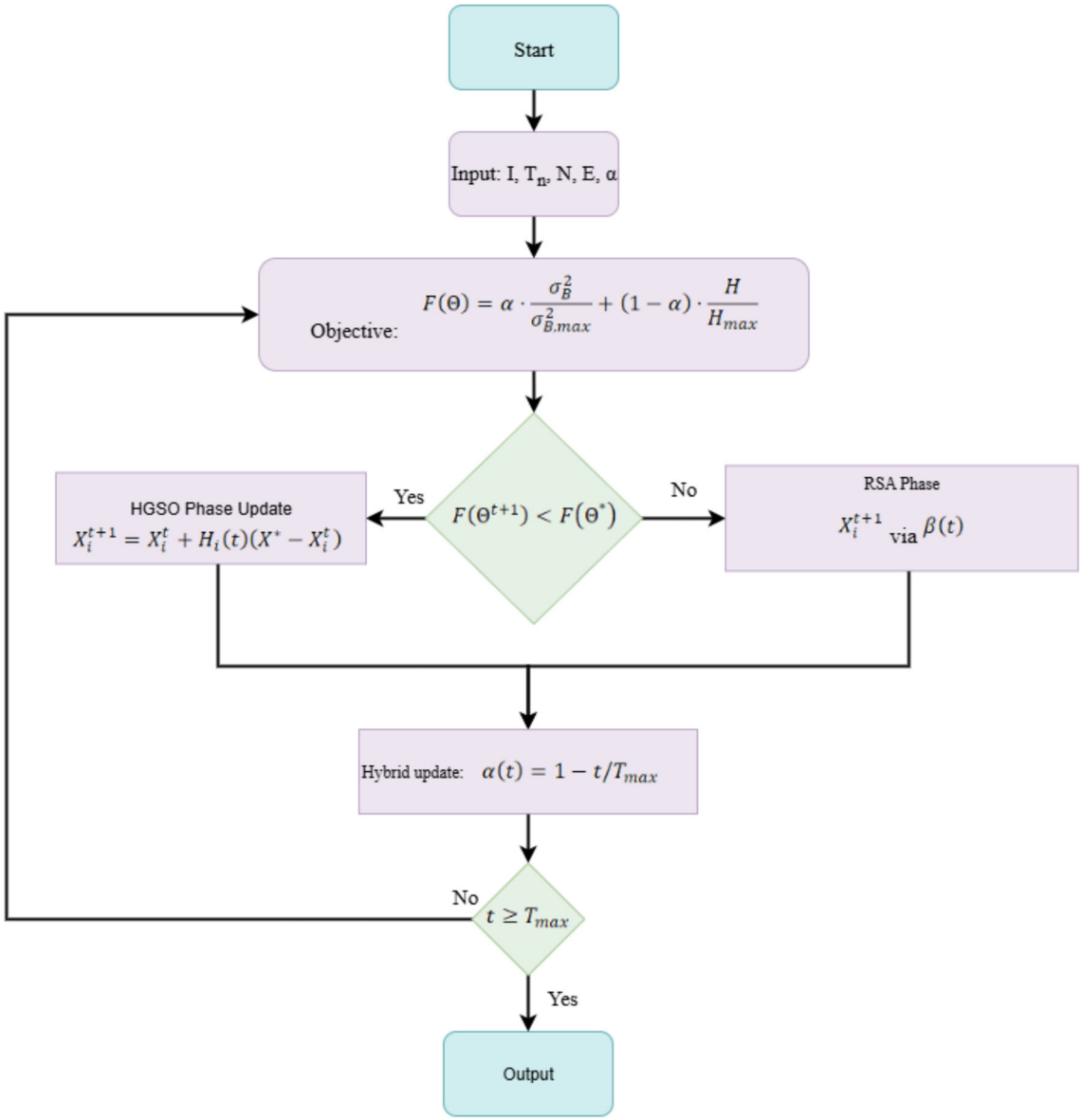

Fig. 2 Flowchart of the proposed method

4 Experimental results

In this section, the experiments of the proposed RSA-HGSO hybrid adaptive algorithm are conducted to evaluate the segmentation performance of satellite imagery. Comparative analyses are performed against GWO, PSO, RSA, HGSO, and the recently reported high-performing MSO [44] algorithm. For this study, color satellite images from the NASA Visible Earth dataset [46] are utilized. The dataset comprises high-resolution (720×480) color images representing diverse geographical regions and various ecological systems. For a fair evaluation, the test phase employed a set of 100 images covering diverse land types, including agricultural areas, forest cover, water bodies, and densely urbanized regions. This diversity allows for an objective assessment of the algorithm's segmentation performance not only in homogeneous but also in complex and multi-component scenes. The key variables analyzed include histogram intensity distributions based on color channels, brightness levels, and spectral characteristics that vary across land-cover types. Consequently, the tested population provides a rich evaluation environment in terms of not only visual diversity but also structural and statistical complexity. Since metaheuristic thresholding methods are not trained on data, unlike deep learning models, data augmentation was applied solely to expand the dataset and was not employed during the optimization phase. All images were normalized to the intensity range [0,1] to reduce computational overhead.

Table 1 Parameter settings of the algorithms used

Algorithm	Parameter
GWO	a: 2 → 0 (linear decreasing)
PSO	w: [0,1], c1: [1, 3], c2: [1, 3]
RSA	β: dynamic (2 × exp(-2 × iteration/epoch) × sin(2π × iteration /epoch))
HGSO	c_1, c_2, c_3: [0,2]
MSO	c1: dynamic (2 × random), c2: dynamic (2 × random), c3: dynamic (2 × random)
RSA-HGSO (Proposed)	β: dynamic (2 × exp(-2 × iteration/epoch) × sin(2π × iteration /epoch)), c_1, c_2, c_3: [0,2]

Table 2 Specifications of used software versions, hardware

Specification	Details
Operating System	Windows 10- 64 bit
Python Version	3.10
CPU	i5-1235U CPU 1.30 GHz

4.1 Experiment setup

In this study, the range of thresholds T = 2–26, which is most frequently adopted in the literature for multi-level image thresholding problems, is considered. Lower threshold levels (T < 2) provide limited discriminative information, while higher levels (T > 26) fail to produce meaningful subregions and unnecessarily increase computational cost. Therefore, the selected range is consistent with common usage in the literature and adequately represents realistic remote sensing segmentation scenarios. The number of iterations is fixed at 100 for all experiments. Preliminary tests showed that convergence tendencies of the algorithms become evident within 80–100 iterations, and improvements beyond 100 iterations remain marginal. Thus, fair comparison across algorithms is ensured while keeping computational costs under control. The population size is set to 50 for all algorithms, and each experiment is conducted with 10 independent runs to evaluate the variance arising from their stochastic nature. The parameter settings of the employed metaheuristic algorithms are summarized in Table 1. In the GWO algorithm, the parameter 'a' is decreased linearly from 2 to 0 across iterations, as widely recommended in the literature, to balance exploration and exploitation. In the PSO algorithm, the inertia weight www is defined within the range [0,1], while the cognitive and social coefficients c_1 and c_2 are defined in the range [1, 3]. In the RSA algorithm, the parameter β, which controls exploration behavior, is dynamically updated using the $\beta = \exp\left(-2 \times \frac{iteration}{epoch}\right) \times \sin\left(2\pi \frac{iteration}{epoch}\right)$. In the HGSO algorithm, the coefficients c_1, c_2, and c_3 used in solution updates are selected within the range [0,2]. In the MSO algorithm, the coefficients c_1, c_2, and c_3 are determined dynamically in the form (2 × random) at each iteration. The proposed RSA–HGSO hybrid algorithm integrates the dynamic β mechanism of RSA with the coefficient settings c_1, c_2, and c_3 of HGSO. Moreover, preliminary sensitivity analyses within the range [0.3–0.9] determined the transition rate λ as 0.7, one of the key parameters of the algorithm. The coefficient α in the hybrid objective function F_{hybrid}, Eq. 3 balances the respective contributions of Otsu's between-class variance and Kapur's entropy. In our experimental studies, this coefficient is fixed at $\alpha = 0.5$. This choice implies that equal weight is assigned to Otsu's objective of maximizing inter-class separability and Kapur's objective of maximizing information content. The sensitivity of performance to different α values is addressed as a limitation in Sect. 6 (Limitation). The detailed hardware and software specifications are summarized in Table 2. All computations are performed in a serial processing manner, allowing a realistic comparison of the computational loads across different algorithms.

4.2 Results

The PSNR performance of the hybrid adaptive RSA-HGSO algorithm was evaluated based on different threshold levels for the test images. The results demonstrate that RSA-HGSO achieves competitive and, in many cases, superior performance compared to other algorithms across various threshold levels. The PSNR comparison for all algorithms is summarized in Table 3 and illustrated in Fig. 3. For the Satellite_1 image, RSA-HGSO achieves a PSNR of 18.8341 at 26 threshold levels. This value is remarkably close to those obtained by classical RSA (18.8477), HGSO (18.6619), GWO (18.7649), PSO (18.6523), and MSO (18.7477) at the same threshold level. Although the difference between RSA and RSA-HGSO is minimal at higher thresholds, RSA-HGSO exhibits notably better performance at lower thresholds, for instance at threshold 6 (17.8501 vs RSA 17.0454). In the case of Satellite_2, RSA-HGSO achieves its highest PSNR performance of 27.3904 at 26 thresholds, which is highly competitive when compared to RSA (27.5208), HGSO (27.3587), GWO (27.2508), PSO (27.3330), and MSO (26.4168) at the same threshold level. At medium threshold levels, RSA-HGSO (26.7294 at threshold 14) demonstrates either superior or equivalent performance relative to classical RSA (26.6187) and the other algorithms. For Satellite_3, RSA-HGSO attains a PSNR of 32.7631 at 26 thresholds, which is very close to RSA (32.8187), PSO (32.9201), GWO (32.8800), and HGSO (32.3094), indicating competitive overall performance. At lower and medium thresholds, RSA-HGSO also approaches

Table 3 PSNR statistics for each algorithm across test images and threshold levels

Image	Threshold	GWO	PSO	RSA	HGSO	MSO	RSA-HGSO
Satellite_1	2	13.5713	13.6072	13.6072	13.6048	13.6072	13.6072
	6	17.0407	17.1565	17.0454	16.9690	16.8188	17.8501
	10	18.3382	18.3023	18.3996	18.3866	18.0486	18.2342
	14	18.5433	18.6470	18.3906	18.7174	18.5135	18.3982
	18	18.5771	18.5076	18.6493	18.6970	18.6824	18.7881
	22	18.7408	18.7740	18.8362	18.5604	18.7461	18.8136
	26	18.7649	18.6523	18.8477	18.6619	18.7477	18.8341
Satellite_2	2	16.6058	16.6058	16.6058	16.6058	16.6058	16.6058
	6	22.1830	23.5573	23.7995	23.3095	23.0995	23.8101
	10	25.7266	25.3816	25.7501	25.4130	25.6554	25.5604
	14	26.0385	26.6222	26.6187	26.4097	26.6047	26.7294
	18	26.9741	27.0646	27.1925	26.9892	26.3720	26.7578
	22	26.7080	27.1822	27.3351	27.2120	26.0674	27.3109
	26	27.2508	27.3330	27.5208	27.3587	26.4168	27.3904
Satellite_3	2	17.1542	17.1542	17.1542	17.0435	17.1542	17.1542
	6	25.1074	25.3454	25.7224	24.9428	25.0949	24.6397
	10	28.9063	28.9060	28.7479	28.6907	27.7492	28.3977
	14	30.3628	30.9277	30.2139	30.0850	30.6346	30.4343
	18	31.1867	31.2771	31.5626	29.4463	31.6227	31.4897
	22	31.6128	32.6287	32.1186	30.9073	31.0810	31.7158
	26	32.8800	32.9201	32.8187	32.3094	32.6633	32.7631
Satellite_4	2	16.4771	16.4771	16.4771	16.2867	16.4771	16.4771
	6	22.2639	22.4042	22.2531	21.4877	21.5297	22.0130
	10	24.2448	24.2297	24.1117	24.2797	24.2050	24.1417
	14	24.9836	24.8566	24.8259	24.5986	24.3572	24.8795
	18	25.1184	25.0259	25.0500	24.9542	25.0627	24.6584
	22	24.9275	25.0927	25.0494	24.7760	24.7944	25.2215
	26	25.0611	25.3280	25.3243	25.1794	24.8727	25.2050
Satellite_5	2	16.0215	16.0215	16.0215	15.7629	16.0215	16.0215
	6	20.3344	20.3109	20.2903	20.0544	20.3780	20.3106
	10	21.0098	21.0872	21.1355	20.6775	20.9881	21.1093
	14	21.4255	21.5063	21.4874	21.3939	21.2804	21.4891
	18	21.5037	21.5789	21.5741	21.4457	21.5747	21.5586
	22	21.6131	21.6224	21.6267	21.6091	21.4320	21.6347
	26	21.5028	21.6767	21.6536	21.6515	21.5282	21.6801
Satellite_6	2	15.7473	15.7473	15.7473	15.7735	15.7473	15.7473
	6	20.4006	20.3146	20.4721	20.2033	20.2465	20.4620
	10	21.0126	21.1114	21.0268	20.7932	20.7902	21.1117
	14	21.2976	21.3992	21.4282	21.3390	21.3649	21.3924
	18	21.5278	21.5277	21.4794	21.4382	21.4530	21.4747
	22	21.4729	21.5548	21.5609	21.4913	21.4322	21.4117
	26	21.5770	21.5793	21.6067	21.5337	21.5946	21.5822

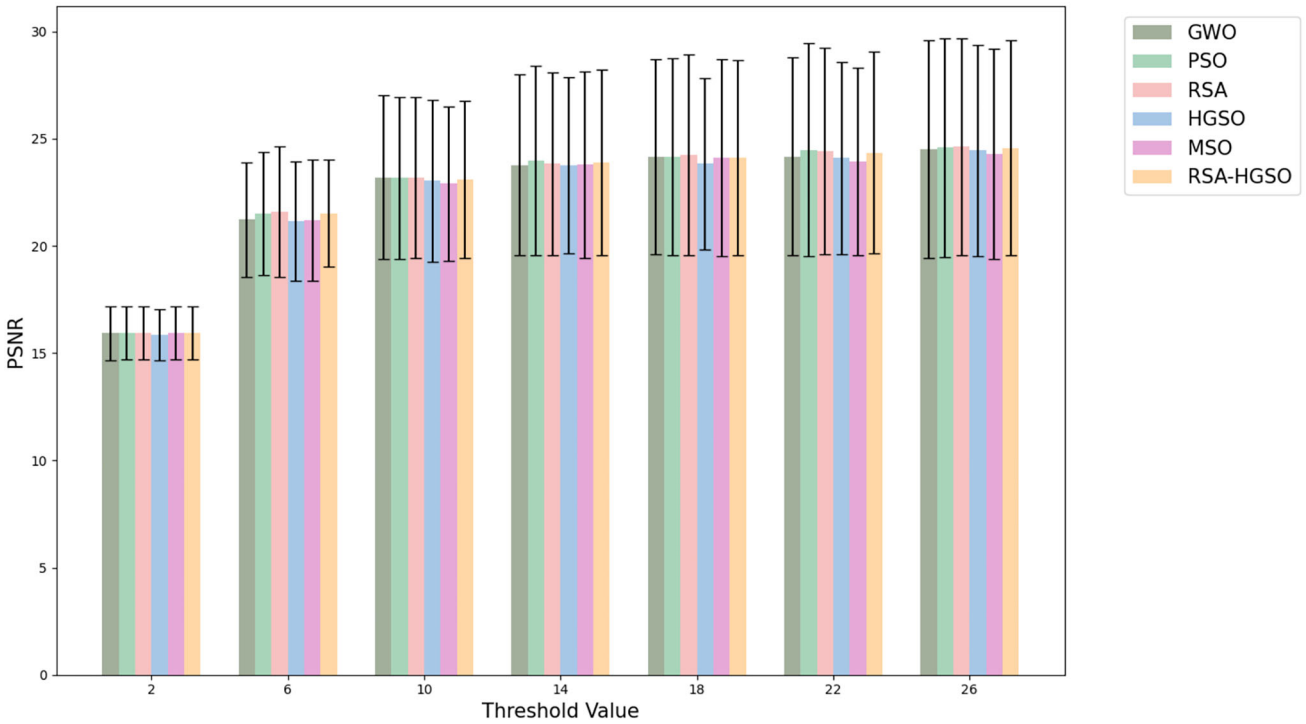

Fig. 3 PSNR performance according to algorithms

RSA's performance, e.g., at threshold 10 (28.3977 vs RSA 28.7479). In Satellite_4, RSA-HGSO achieves its best result at threshold 22 with a PSNR of 25.2215, outperforming RSA (25.0494), PSO (25.0927), and GWO (24.9275). For Satellite_5 and Satellite_6, RSA-HGSO provides PSNR values of 21.6801 and 21.5822 at 26 thresholds, respectively, offering performance equivalent to or exceeding other algorithms. For example, for Satellite_5, classical RSA achieves 21.6536 and PSO 21.6767, while RSA-HGSO demonstrates a slightly superior result. Overall, RSA-HGSO competes effectively with classical RSA and other widely used MH algorithms in terms of PSNR. The strong performance at low and medium thresholds highlights the algorithm's effectiveness in enhancing segmentation quality, while the minor differences at higher thresholds indicate balanced and consistent performance. Consequently, RSA-HGSO achieves an effective balance between efficiency and quality in multilevel image thresholding optimization, delivering particularly strong results at low and medium thresholds. These characteristics make it a reliable and effective method for satellite image segmentation.

SSIM performance of the hybrid adaptive RSA-HGSO algorithm is analyzed in detail for each satellite image based on threshold levels. A comparative summary of the SSIM values for all algorithms is presented in Table 4 and illustrated in Fig. 4. For the Satellite_1 image, RSA-HGSO achieves its best performance at a threshold level of 26, attaining an SSIM value of 0.8512. At this level, classical RSA records 0.8506, HGSO 0.8349, GWO 0.8440, PSO 0.8364, and MSO 0.8452. RSA-HGSO therefore demonstrates both higher and competitive structural similarity compared to the other algorithms. Notably, it provides a pronounced advantage at lower threshold levels (e.g., threshold 6: RSA-HGSO 0.7704, RSA 0.7469, HGSO 0.7405). For Satellite_2, RSA-HGSO achieves 0.8490 SSIM at threshold 26, while classical RSA, HGSO, PSO, GWO, and MSO reach 0.8598, 0.8545, 0.8499, 0.8368, and 0.8066, respectively. At intermediate threshold levels (14–18), RSA-HGSO (e.g., threshold 14: 0.7971; threshold 18: 0.8057) remains competitive with classical RSA and other algorithms, occasionally providing superior performance. In the case of Satellite_3, RSA-HGSO attains an SSIM of 0.9657 at the highest threshold level (26), surpassing RSA (0.9638), PSO (0.9617), GWO (0.9614), and HGSO (0.9570). At intermediate thresholds (e.g., threshold 14: RSA-HGSO 0.9224, RSA 0.9164, GWO 0.9160), the algorithm continues to deliver robust and consistent structural similarity. For Satellite_4, Satellite_5, and Satellite_6, RSA-HGSO achieves its most efficient SSIM values at thresholds 22, 26, and 26, respectively. For Satellite_4, the highest SSIM is 0.9648 at threshold 22, slightly outperforming RSA (0.9626), PSO (0.9633), and HGSO and GWO (around 0.96). For Satellite_5 at threshold 26, RSA-HGSO reaches 0.9125, with RSA and PSO achieving 0.9128 and 0.9122, respectively. Similarly, for Satellite_6 at threshold 26, RSA-HGSO obtains 0.9037, while RSA and PSO record 0.9100 and 0.9033, respectively. In summary, the

Table 4 SSIM statistics for each algorithm across test images and threshold levels

Image	Threshold	GWO	PSO	RSA	HGSO	MSO	RSA-HGSO
Satellite_1	2	0.5816	0.5825	0.5825	0.5821	0.5825	0.5825
	6	0.7473	0.7505	0.7469	0.7405	0.7384	0.7704
	10	0.8037	0.8016	0.8097	0.8106	0.7905	0.7941
	14	0.8240	0.8301	0.8110	0.8338	0.8198	0.8124
	18	0.8274	0.8241	0.8360	0.8328	0.8332	0.8427
	22	0.8428	0.8438	0.8498	0.8270	0.8418	0.8475
	26	0.8440	0.8364	0.8506	0.8349	0.8452	0.8512
Satellite_2	2	0.3882	0.3882	0.3882	0.3882	0.3882	0.3882
	6	0.5854	0.6220	0.6283	0.6139	0.6073	0.6311
	10	0.7286	0.7205	0.7317	0.7076	0.7239	0.7242
	14	0.7593	0.7902	0.7883	0.7771	0.7849	0.7971
	18	0.8192	0.8239	0.8301	0.8162	0.7896	0.8057
	22	0.8128	0.8325	0.8497	0.8375	0.7928	0.8416
	26	0.8368	0.8499	0.8598	0.8545	0.8066	0.8490
Satellite_3	2	0.4840	0.4840	0.4840	0.4816	0.4840	0.4840
	6	0.7790	0.7844	0.7933	0.7709	0.7790	0.7687
	10	0.8832	0.8832	0.8788	0.8795	0.8569	0.8697
	14	0.9160	0.9278	0.9164	0.9111	0.9242	0.9224
	18	0.9319	0.9353	0.9464	0.8972	0.9437	0.9384
	22	0.9393	0.9581	0.9539	0.9273	0.9307	0.9416
	26	0.9614	0.9617	0.9638	0.9570	0.9622	0.9657
Satellite_4	2	0.7964	0.7964	0.7964	0.7917	0.7964	0.7964
	6	0.9258	0.9278	0.9256	0.9155	0.9162	0.9227
	10	0.9517	0.9517	0.9503	0.9516	0.9523	0.9508
	14	0.9611	0.9595	0.9602	0.9564	0.9535	0.9595
	18	0.9631	0.9628	0.9614	0.9614	0.9620	0.9581
	22	0.9613	0.9633	0.9626	0.9597	0.9599	0.9648
	26	0.9636	0.9661	0.9653	0.9637	0.9607	0.9643
Satellite_5	2	0.6033	0.6033	0.6033	0.6003	0.6033	0.6033
	6	0.8072	0.8051	0.8076	0.7881	0.8084	0.8055
	10	0.8530	0.8579	0.8633	0.8397	0.8527	0.8593
	14	0.8872	0.8941	0.8901	0.8773	0.8763	0.8876
	18	0.8955	0.9037	0.9036	0.8904	0.9026	0.8983
	22	0.9043	0.9076	0.9076	0.9056	0.8933	0.9067
	26	0.8975	0.9122	0.9128	0.9092	0.9025	0.9125
Satellite_6	2	0.4920	0.4920	0.4920	0.4927	0.4920	0.4920
	6	0.7670	0.7619	0.7712	0.7541	0.7623	0.7704
	10	0.8305	0.8390	0.8302	0.8114	0.8207	0.8395
	14	0.8631	0.8770	0.8816	0.8679	0.8722	0.8769
	18	0.8982	0.8953	0.8902	0.8856	0.8805	0.8899
	22	0.8849	0.8979	0.9008	0.8888	0.8819	0.8778
	26	0.9021	0.9033	0.9100	0.9004	0.9100	0.9037

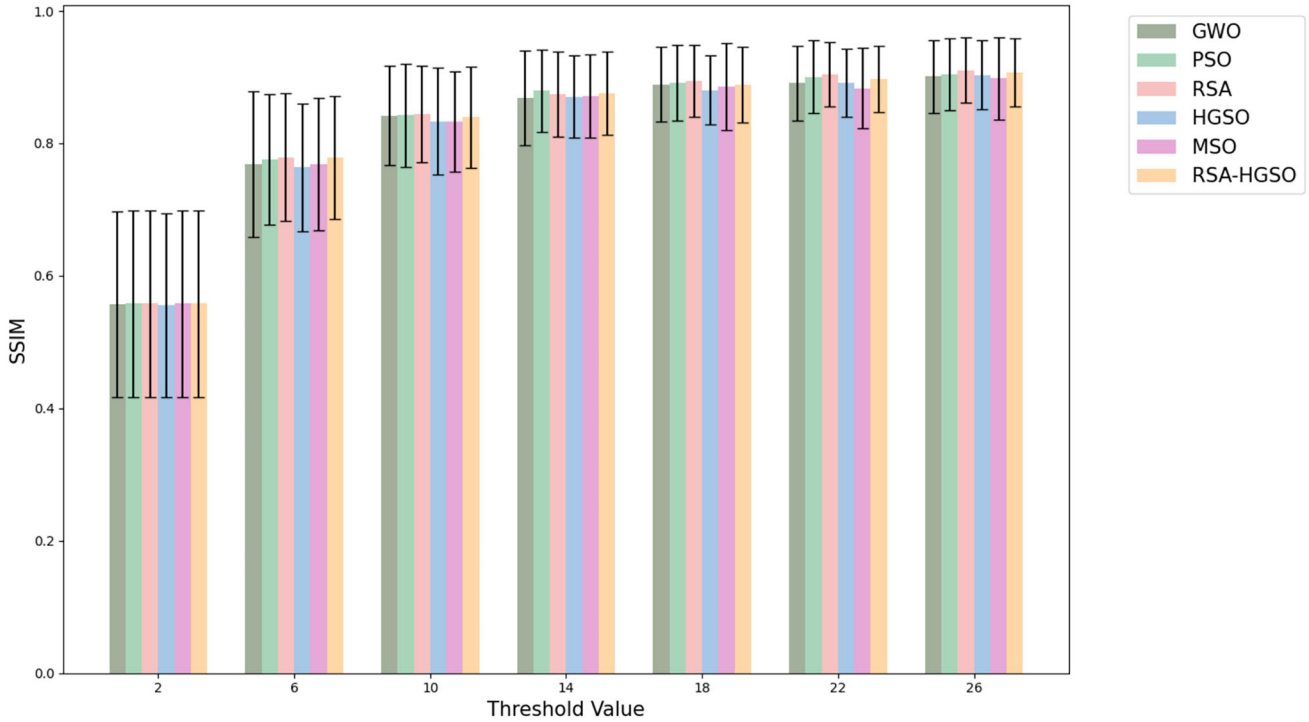

Fig. 4 SSIM performance according to algorithms

hybrid adaptive RSA-HGSO algorithm provides high structural similarity values at low and intermediate thresholds, outperforming other algorithms for the thresholds where it achieves the highest SSIM. At higher thresholds, it remains competitive with classical RSA and PSO, generally producing comparable results. These findings demonstrate that RSA-HGSO is a reliable and competitive approach for both structure preservation and satellite image segmentation.

The Feature Similarity Index (FSIM) performance of the hybrid adaptive RSA-HGSO algorithm is summarized in Table 5 and illustrated in Fig. 5. Based on the threshold levels across each satellite image, the algorithm demonstrates robust and competitive results compared to other methods. For the Satellite_1 image, RSA-HGSO achieves a FSIM value of 0.9349 at 26 thresholds, highlighting its competitive performance. At the same threshold level, RSA, HGSO, GWO, PSO, and MSO yield 0.9342, 0.9149, 0.9400, 0.9346, and 0.9376, respectively. Although GWO and MSO present slightly higher FSIM values, RSA-HGSO demonstrates more efficient performance at intermediate thresholds (e.g., 14 thresholds: 0.8701) compared to several algorithms. In the Satellite_2 image, RSA-HGSO achieves its best FSIM value of 0.8089 at 26 thresholds. At the same level, RSA, HGSO, PSO, GWO, and MSO attain 0.8374, 0.8234, 0.8526, 0.8029, and 0.7877, respectively. While PSO and RSA exhibit slightly better FSIM scores at this level, RSA-HGSO maintains consistent and strong feature similarity, particularly at medium and higher thresholds. For Satellite_3, RSA-HGSO demonstrates an effective performance with a FSIM score of 0.94333 at 26 thresholds. In comparison, RSA, PSO, GWO, MSO, and HGSO record 0.9430, 0.9428, 0.9425, 0.9390, and 0.9246, respectively, confirming RSA-HGSO's competitiveness and high quality. In the Satellite_4 image, RSA-HGSO reaches a FSIM value of 0.9802 at 22 thresholds, outperforming RSA (0.9751), PSO (0.9791), GWO (0.9736), HGSO (0.9735), and MSO (0.9718). Particularly around the 22-threshold level, RSA-HGSO provides more efficient results compared to the competing algorithms. For Satellite_5 and Satellite_6, RSA-HGSO achieves FSIM values of 0.9426 and 0.9360 at 26 thresholds, maintaining high image quality with improved performance. At similar thresholds, RSA and PSO record 0.9390 and 0.9402 for Satellite_5, while HGSO scores 0.9306. For Satellite_6, RSA, PSO, GWO, and HGSO achieve 0.9399, 0.9369, 0.9328, and 0.9336, respectively. These results indicate that RSA-HGSO is particularly consistent and competitive in feature similarity at higher threshold levels. In conclusion, the hybrid adaptive RSA-HGSO algorithm delivers high and stable FSIM performance for satellite image segmentation. Its advantage lies in preserving critical features and enhancing image quality, especially at medium and high thresholds. Compared to other algorithms, RSA-HGSO produces competitive, and in some cases superior, outcomes, confirming its effectiveness and reliability in multi-level thresholding problems.

Table 5 FSIM statistics for each algorithm across test images and threshold levels

Image	Threshold	GWO	PSO	RSA	HGSO	MSO	RSA-HGSO
Satellite_1	2	0.5611	0.5607	0.5607	0.5605	0.5607	0.5607
	6	0.7584	0.7623	0.7577	0.7546	0.7543	0.7689
	10	0.8419	0.8399	0.8384	0.8404	0.8290	0.8200
	14	0.8869	0.8847	0.8656	0.8679	0.8670	0.8701
	18	0.9049	0.9121	0.9046	0.8941	0.8886	0.8980
	22	0.9285	0.9251	0.9273	0.9088	0.9239	0.9178
	26	0.9400	0.9346	0.9342	0.9149	0.9376	0.9349
Satellite_2	2	0.1305	0.1305	0.1305	0.1305	0.1305	0.1305
	6	0.3909	0.4077	0.3947	0.3943	0.3870	0.4064
	10	0.5775	0.5810	0.5774	0.5332	0.5755	0.5609
	14	0.6442	0.7030	0.6823	0.6602	0.6806	0.6647
	18	0.7703	0.7701	0.7457	0.7202	0.7318	0.7394
	22	0.7806	0.8037	0.7980	0.7746	0.7677	0.7762
	26	0.8029	0.8526	0.8374	0.8234	0.7877	0.8089
Satellite_3	2	0.3249	0.3249	0.3249	0.3252	0.3249	0.3249
	6	0.6556	0.6564	0.6538	0.6416	0.6553	0.6503
	10	0.8064	0.8070	0.8023	0.7771	0.7705	0.7780
	14	0.8705	0.8727	0.8520	0.8448	0.8595	0.8539
	18	0.9065	0.8988	0.8954	0.8558	0.9064	0.8861
	22	0.9026	0.9300	0.9153	0.8906	0.8996	0.9156
	26	0.9425	0.9428	0.9430	0.9246	0.9390	0.9433
Satellite_4	2	0.7533	0.7533	0.7533	0.7509	0.7533	0.7533
	6	0.9112	0.9135	0.9113	0.9005	0.9019	0.9076
	10	0.9521	0.9509	0.9493	0.9482	0.9524	0.9480
	14	0.9684	0.9665	0.9703	0.9645	0.9554	0.9652
	18	0.9766	0.9773	0.9702	0.9726	0.9739	0.9664
	22	0.9736	0.9791	0.9751	0.9735	0.9718	0.9802
	26	0.9798	0.9842	0.9818	0.9789	0.9745	0.9795
Satellite_5	2	0.4867	0.4867	0.4867	0.4867	0.4867	0.4867
	6	0.7586	0.7552	0.7600	0.7356	0.7584	0.7555
	10	0.8352	0.8401	0.8428	0.8153	0.8384	0.8445
	14	0.8929	0.8958	0.8866	0.8732	0.8781	0.8797
	18	0.9057	0.9250	0.9211	0.9057	0.9134	0.9062
	22	0.9179	0.9341	0.9286	0.9239	0.9228	0.9258
	26	0.9239	0.9401	0.9390	0.9306	0.9317	0.9426
Satellite_6	2	0.3974	0.3974	0.3974	0.3977	0.3974	0.3974
	6	0.7274	0.7263	0.7171	0.7199	0.7281	0.7252
	10	0.8280	0.8351	0.8206	0.8015	0.8217	0.8303
	14	0.8714	0.8846	0.8824	0.8750	0.8757	0.8788
	18	0.9170	0.9165	0.8968	0.8865	0.8901	0.9004
	22	0.9123	0.9246	0.9219	0.9128	0.9153	0.8980
	26	0.9328	0.9369	0.9399	0.9336	0.9428	0.9360

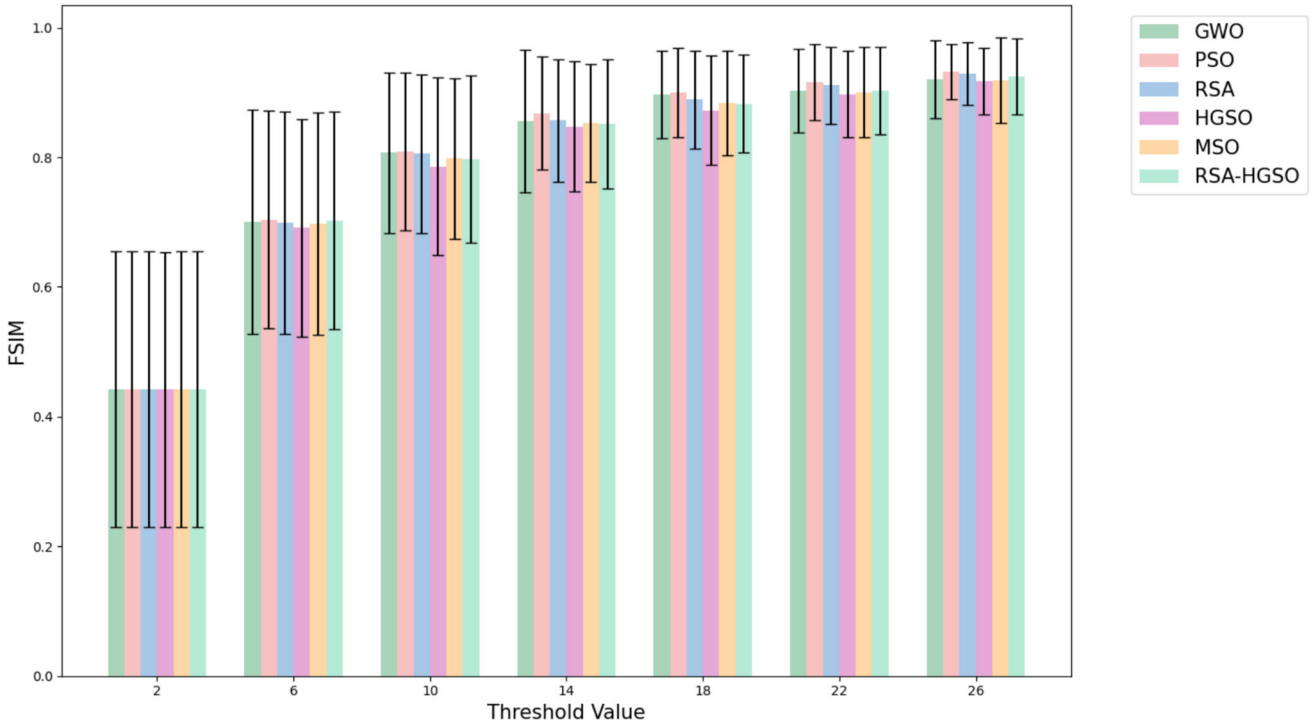

Fig. 5 FSIM performance according to algorithms

The performance of the hybrid adaptive RSA-HGSO algorithm with respect to the Normalized Correlation Coefficient (NCC) is summarized in Table 6. When the satellite images are analyzed based on threshold levels, the Satellite_1 image shows that RSA-HGSO achieves an effective performance at the highest threshold level of 26 with an NCC value of 0.9146. At this level, the classical RSA, HGSO, GWO, PSO, and MSO algorithms yield comparable values of 0.9148, 0.9117, 0.9134, 0.9117, and 0.9130, respectively. At lower and medium threshold levels, RSA-HGSO exhibits relatively stronger performance; for instance, at six thresholds, it achieves 0.8969 compared to 0.8896 for RSA and slightly higher values than the other algorithms. For the Satellite_2 image, RSA-HGSO provides competitive results at higher threshold levels. At 26 thresholds, it achieves an NCC of 0.9885, which is remarkably close to RSA (0.9888), HGSO (0.9884), PSO (0.9885), GWO (0.9882), and MSO (0.9866). This demonstrates the algorithm's stability and high capacity in preserving structural correlation. In the Satellite_3 image, RSA-HGSO stands out at 26 thresholds with an NCC value of 0.9969, competing closely with RSA (0.9969), PSO (0.9970), GWO (0.9969), HGSO (0.9965), and MSO (0.9967). At medium threshold levels, RSA-HGSO also offers strong correlation values ranging between 0.9919 and 0.9958. For the Satellite_4 image, the best NCC performance is obtained by RSA-HGSO at 22 thresholds with a value of 0.9816, closely followed by RSA (0.9810), PSO (0.9812), and GWO (0.9804). In Satellite_5 and Satellite_6, RSA-HGSO maintains competitive or slightly superior performance with NCC values of 0.9586 and 0.9570 at 26 thresholds, respectively. Overall, the hybrid adaptive RSA-HGSO algorithm consistently delivers high and stable correlation values across low, medium, and high threshold levels in all tested satellite images according to the NCC metric. Compared with classical RSA and other modern algorithms, RSA-HGSO preserves both structural consistency and segmentation quality at a high level, demonstrating competitive performance. These findings indicate that RSA-HGSO is a strong and reliable approach for multilevel thresholding tasks in terms of structural and content integrity.

Table 7 compares the performance metrics (PSNR, SSIM, FSIM, and NCC) of the proposed Hybrid RSA-HGSO algorithm with those of RSA, HGSO, GWO, PSO, and MSO. The PSNR value for RSA-HGSO is 24.5927, while the corresponding values for the other algorithms are 24.5785 (RSA), 24.4275 (HGSO), 24.3022 (GWO), 24.4826 (PSO), and 24.4287 (MSO). The SSIM values are 0.9088 for RSA-HGSO and range from 0.9087 to 0.8997 for the other algorithms, whereas FSIM values lie between 0.9233 and 0.9271, and NCC values range from 0.9654 to 0.9663. According to the results of the Wilcoxon signed-rank tests, the significance levels for all metrics are $p \geq 0.15$, indicating that no statistically significant differences were observed in any comparison. These results demonstrate that the Hybrid

Table 6 NCC statistics for each algorithm across test images and threshold levels

Image	Threshold	GWO	PSO	RSA	HGSO	MSO	RSA-HGSO
Satellite_1	2	0.8484	0.8482	0.8482	0.8482	0.8482	0.8482
	6	0.8895	0.8901	0.8896	0.8870	0.8880	0.8969
	10	0.9063	0.9060	0.9065	0.9062	0.9026	0.9045
	14	0.9094	0.9112	0.9078	0.9122	0.9090	0.9076
	18	0.9106	0.9094	0.9112	0.9121	0.9118	0.9136
	22	0.9129	0.9136	0.9147	0.9102	0.9131	0.9142
	26	0.9134	0.9117	0.9148	0.9117	0.9130	0.9146
Satellite_2	2	0.9241	0.9241	0.9241	0.9241	0.9241	0.9241
	6	0.9724	0.9759	0.9765	0.9744	0.9749	0.9766
	10	0.9839	0.9832	0.9840	0.9826	0.9837	0.9832
	14	0.9851	0.9866	0.9865	0.9858	0.9864	0.9866
	18	0.9876	0.9878	0.9880	0.9874	0.9863	0.9870
	22	0.9871	0.9881	0.9883	0.9880	0.9858	0.9883
	26	0.9882	0.9885	0.9888	0.9884	0.9866	0.9885
Satellite_3	2	0.9347	0.9347	0.9347	0.9348	0.9347	0.9347
	6	0.9851	0.9854	0.9855	0.9840	0.9849	0.9843
	10	0.9929	0.9929	0.9928	0.9921	0.9912	0.9919
	14	0.9949	0.9953	0.9945	0.9944	0.9949	0.9947
	18	0.9958	0.9957	0.9959	0.9942	0.9960	0.9958
	22	0.9960	0.9968	0.9964	0.9955	0.9957	0.9962
	26	0.9969	0.9970	0.9969	0.9965	0.9967	0.9969
Satellite_4	2	0.9198	0.9198	0.9198	0.9196	0.9198	0.9198
	6	0.9687	0.9690	0.9687	0.9658	0.9671	0.9682
	10	0.9775	0.9775	0.9770	0.9771	0.9772	0.9767
	14	0.9805	0.9801	0.9798	0.9790	0.9783	0.9800
	18	0.9812	0.9809	0.9809	0.9805	0.9809	0.9797
	22	0.9804	0.9812	0.9810	0.9802	0.9802	0.9816
	26	0.9811	0.9820	0.9820	0.9814	0.9806	0.9816
Satellite_5	2	0.8940	0.8940	0.8940	0.8931	0.8940	0.8940
	6	0.9465	0.9464	0.9462	0.9446	0.9465	0.9465
	10	0.9534	0.9539	0.9536	0.9515	0.9531	0.9535
	14	0.9566	0.9570	0.9567	0.9558	0.9555	0.9567
	18	0.9571	0.9578	0.9577	0.9568	0.9576	0.9575
	22	0.9580	0.9582	0.9582	0.9579	0.9571	0.9582
	26	0.9575	0.9587	0.9584	0.9584	0.9576	0.9586
Satellite_6	2	0.8902	0.8902	0.8902	0.8905	0.8902	0.8902
	6	0.9455	0.9450	0.9444	0.9435	0.9445	0.9452
	10	0.9520	0.9527	0.9518	0.9499	0.9508	0.9522
	14	0.9543	0.9551	0.9553	0.9546	0.9548	0.9550
	18	0.9564	0.9564	0.9559	0.9554	0.9557	0.9558
	22	0.9561	0.9567	0.9567	0.9560	0.9558	0.9555
	26	0.9569	0.9570	0.9572	0.9564	0.9570	0.9570

Table 7 Performance comparison of Hybrid RSA-HGSO with other algorithms and Wilcoxon tests

Metrics	GWO	PSO	RSA	HGSO	MSO	RSA-HGSO	Wilcoxon test statistic	p-value
PSNR	24.3022	24.4826	24.5785	24.4275	24.4287	24.5927	0.16–0.32	0.52–0.87
SSIM	0.9017	0.9043	0.9087	0.9005	0.8997	0.9088	0.16–0.65	0.51–0.87
FSIM	0.9233	0.9258	0.9271	0.9102	0.9190	0.9233	0.22–1.44	0.15–0.83
NCC	0.9659	0.9659	0.9662	0.9658	0.9654	0.9663	0.16–0.48	0.63–0.87

RSA-HGSO algorithm is statistically equivalent in performance to other MH algorithms. Although small advantages were observed in PSNR and SSIM metrics, these differences were not statistically significant, confirming that the proposed algorithm delivers a balanced and reliable performance.

The overall performance of the algorithms on test images is analyzed and summarized in Table 8, while representative visual outputs are illustrated in Fig. 6. In terms of PSNR averages, the highest value is obtained by RSA-HGSO with 24.5927. This is closely followed by RSA (24.5785) and PSO (24.4826), whereas the other algorithms remain at lower levels: HGSO (24.4275), MSO (24.4287), and GWO (24.3022). Considering the standard deviations, RSA-HGSO exhibits the largest variation with 5.0142, while GWO (4.5519) and HGSO (4.8226) demonstrate lower fluctuations. Thus, although RSA-HGSO achieves the highest mean PSNR, its stability can be considered moderate. For the structural similarity metric (SSIM), RSA-HGSO again demonstrates the best performance with an average value of 0.9088. RSA (0.9087) achieves nearly identical performance, while PSO (0.9043) ranks third. Lower average SSIM values are obtained by GWO (0.9017), HGSO (0.9005), and MSO (0.8997). Regarding standard deviations, RSA-HGSO (0.0506), RSA (0.0501), and GWO (0.0479) provide more stable results, whereas MSO (0.0586) and HGSO (0.0555) yield more fluctuating outputs. For the feature similarity index (FSIM), the highest average value is achieved by RSA (0.9271), followed by PSO (0.9258) and RSA-HGSO (0.9233). GWO (0.9233) remains at a similar level, while MSO (0.9190) and HGSO (0.9102) produce lower results. Standard deviation analysis shows that RSA-HGSO (0.0528) and GWO (0.0453) provide more balanced outcomes in feature preservation, whereas HGSO (0.0659) and RSA (0.0556) exhibit greater variability. In the NCC metric, which evaluates segmentation quality, RSA-HGSO achieves the highest efficiency with 0.9663. It is closely followed by RSA (0.9662), PSO (0.9659), and GWO (0.9659), while HGSO (0.9658) and MSO (0.9654) slightly lag behind. Standard deviation results reveal that RSA-HGSO (0.0299) and GWO (0.0297) show the lowest variability, indicating the highest consistency among all algorithms. According to the analyses presented in Table 8, although the proposed RSA–HGSO algorithm achieves the highest mean PSNR value (24.5927), it also exhibits the largest standard deviation (PSNR: 5.0142) among all the algorithms. This finding may be interpreted as indicating that the method displays the most unstable performance in certain trials. However, this variation arises as a natural consequence of RSA's strong global exploration mechanism, which constitutes a fundamental component of the hybrid structure. RSA's ability to search a wide solution space and avoid local optima increases the likelihood that the algorithm will reach rarer but potentially superior solutions (i.e., those closer to the global optimum) in individual runs. Consequently, while some trials produce outcomes significantly more efficiently than those obtained by the competing algorithms, the inherently stochastic nature of RSA also leads to higher overall variability. In other words, the elevated variance reflects the algorithm's strong potential for superior solutions. Supporting this interpretation, RSA-HGSO delivers the most stable results for structural integrity metrics (SSIM Std.: 0.0506, NCC Std.: 0.0299), demonstrating that the increased variance is confined to the pixel-level PSNR metric and that the algorithm remains consistent in its ability to preserve fundamental structural information. Overall, the hybrid adaptive RSA-HGSO algorithm achieves the best performance in terms of PSNR and NCC averages, while sharing the leading position in SSIM with RSA. Standard deviation analysis further demonstrates that RSA-HGSO provides particularly stable outputs in SSIM and NCC metrics, while also maintaining high consistency in FSIM. Consequently, RSA-HGSO stands out in multi-level satellite image thresholding optimization, offering both high quality and reliable performance.

In addition, to evaluate the information-preservation capability of the proposed RSA–HGSO algorithm after segmentation, statistical analyses were conducted at both the pixel and spatial levels, as presented in Fig. 7. At the global scale, Pearson correlation $r = 0.9557$ and Spearman correlation $\rho = 0.9549$ indicate that the pixel ordering is almost entirely preserved and that the transformation constitutes a largely monotonic and near-linear mapping. The coefficient of determination $r^2 \approx 0.913$ further suggests that approximately 91%

Table 8 Summary of overall algorithm performance

Algorithm	PSNR		SSIM		FSIM		NCC	
	Mean	Std	Mean	Std	Mean	Std	Mean	Std
GWO	24.3022	4.5520	0.9017	0.0479	0.9233	0.0453	0.9659	0.0297
PSO	24.4826	4.9022	0.9043	0.0529	0.9258	0.0542	0.9659	0.0305
RSA	24.5785	4.9874	0.9087	0.0501	**0.9271**	0.0556	0.9662	0.0302
HGSO	24.4275	4.8226	0.9005	0.0555	0.9102	0.0659	0.9658	0.0301
MSO	24.4287	4.9529	0.8997	0.0586	0.9190	0.0545	0.9654	0.0311
RSA-HGSO	**24.5927**	5.0142	**0.9088**	0.0506	0.9233	**0.0528**	**0.9663**	0.0299

The bold values are used solely to highlight the best-performing results for easier comparison. They do not represent any other specific significance or calculation beyond emphasizing the highest values in each respective metric

of the variance in the original intensities is retained in the segmented output. Although banding/quantization artifacts appear at the extreme low and high intensity ranges (0–30 and 220 +), the deviations remain limited. This effect aligns with the inherent characteristics of multi-level thresholding. Intensity maps of neighboring pixel pairs exhibit a pronounced concentration along the diagonal, indicating that local smoothness and edge continuity are largely maintained post-segmentation. Global Pearson $r = 0.8042$ and Spearman $\rho = 0.8051$ values demonstrate that spatial correlation remains high, although naturally lower than pixel-to-pixel correlation. This discrepancy is consistent with a partial flattening of micro-textural variance following thresholding. Nevertheless, the explained variance at $r^2 \approx 0.647$ confirms that neighborhood relationships are substantially preserved. Consistent patterns emerge across all test images: (i) the original–segmented distributions adhere closely to the diagonal within a narrow band; (ii) in 2D neighbor-pixel histograms, the diagonal focus is maintained while grid/banding traces appear due to multi-level thresholding; (iii) in high-intensity texture regions, scatter around the diagonal slightly increases, yet edge continuity remains apparent. These analyses indicate that the algorithm does not disrupt global brightness ranking or local structural information, with its primary effect being the controlled quantization of fine-texture components. The close agreement between Pearson and Spearman coefficients (pixel-level ~ 0.955, neighborhood ~ 0.805) further confirms that the transformation is strongly monotonic and approximately linear in most regions. Collectively, these findings demonstrate that image integrity and diagnostic information are preserved: macrostructures, class boundaries, and edges are maintained, while fine-texture fluctuations are simplified to the expected extent under multi-level thresholding.

4.3 Ablation study: component analysis of RSA-HGSO

An ablation study was conducted to elucidate the contributions of the individual components of the proposed hybrid RSA–HGSO algorithm, namely RSA and HGSO. In this context, three configurations were evaluated: RSA only, HGSO only, and the hybrid RSA–HGSO algorithm. Examination of the PSNR results shows that RSA–HGSO achieves the highest average value of 24.5927 dB, outperforming both RSA alone (24.5785 dB) and HGSO alone (24.4275 dB). Regarding SSIM, the hybrid model attains a value of 0.9088, exceeding the results of both RSA (0.9087) and HGSO (0.9005). While fluctuations in structural similarity values were observed at medium and high threshold levels when RSA and HGSO were applied individually, the hybrid algorithm provides more stable outcomes. FSIM results exhibit a similar trend: HGSO alone achieves a lower mean FSIM of 0.9102, whereas RSA performs at 0.9271. The hybrid RSA-HGSO balances the performance of its constituent algorithms, yielding a more consistent FSIM value of 0.9233. With respect to the NCC metric, RSA-HGSO attains 0.9663, surpassing both RSA (0.9662) and HGSO (0.9658). Although the differences appear modest, Wilcoxon test results confirm that the hybrid algorithm demonstrates statistically more consistent performance compared to its individual components. Overall, these findings indicate that RSA-HGSO not only integrates the individual strengths of RSA and HGSO but also complementarily and adaptively combines the robust exploration capability of RSA with the precise exploitation mechanism of HGSO. Consequently, the hybrid structure produces more stable and higher-quality segmentation outputs, clearly highlighting its methodological contribution.

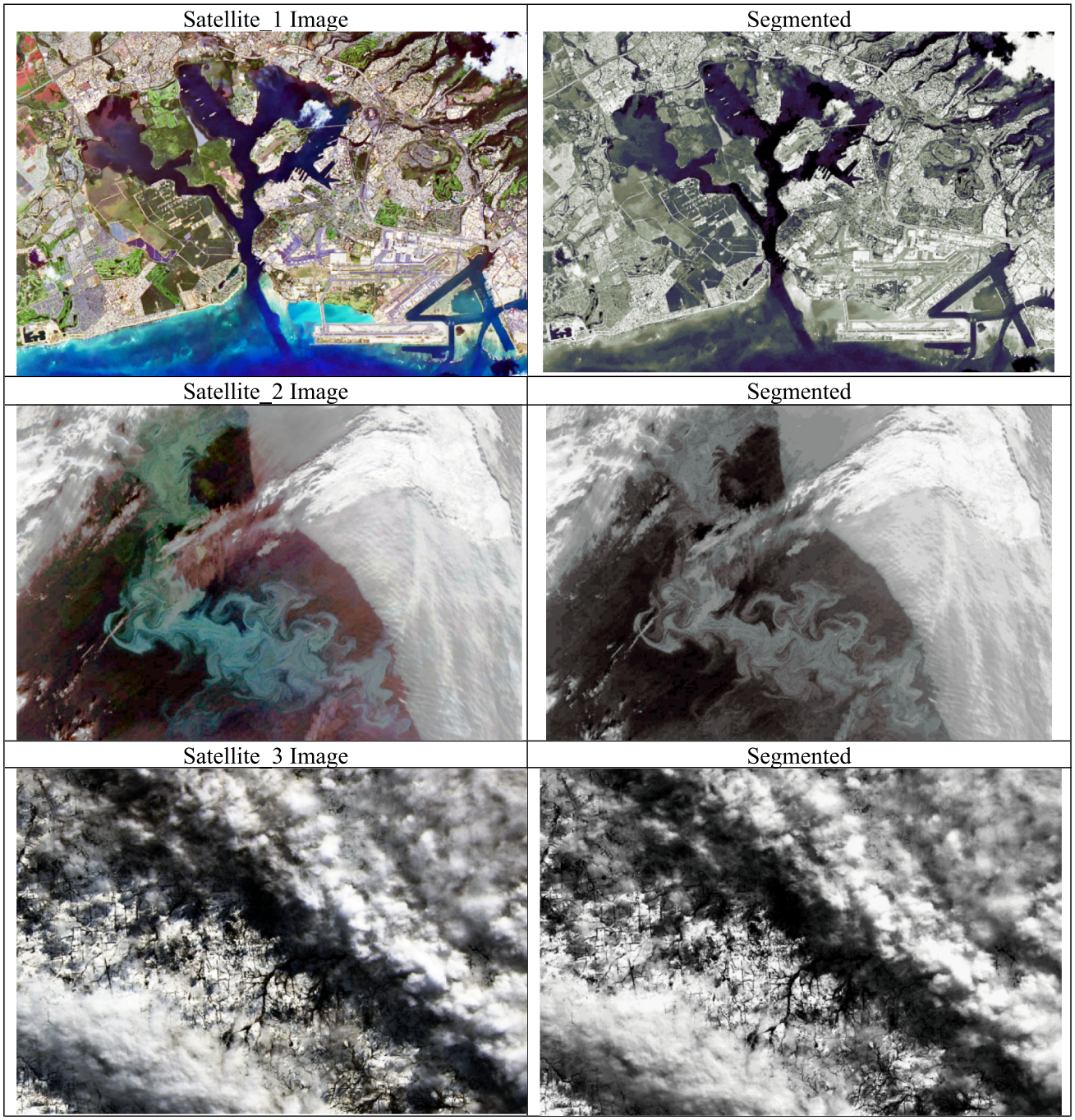

Fig. 6 Visual outcomes on test images

5 Discussion

In this study, the proposed hybrid adaptive RSA-HGSO algorithm is extensively compared with widely used metaheuristics such as GWO, PSO, RSA, HGSO, and MSO for the multi-level satellite image thresholding problem. The Wilcoxon signed-rank test results presented in Table 7 show that $p \geq 0.15$ for all metrics. This finding clearly demonstrates that there is no statistically significant difference between the proposed RSA–HGSO algorithm and other high-performance metaheuristic algorithms (particularly RSA, PSO, and MSO). The algorithm's best mean PSNR (24.5927) and NCC (0.9663) values are considered statistically equivalent to those of the competing methods. This indicates that the hybrid strategy is as reliable and competitive as the most efficient single algorithms yet does not

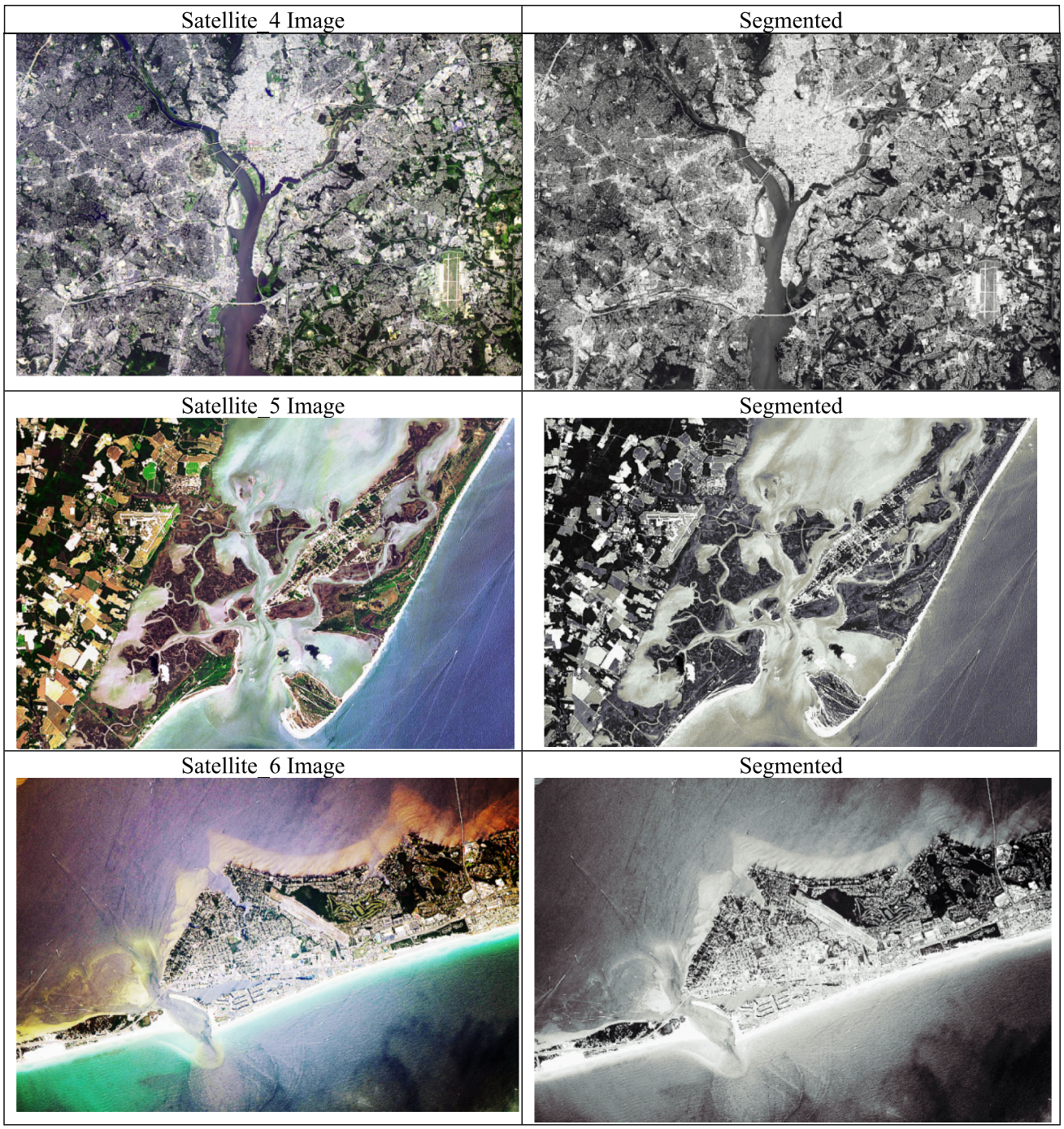

Fig. 6 continued

establish absolute superiority. Accordingly, the strength of RSA–HGSO lies primarily in its ability to balance exploration and exploitation mechanisms in a controlled manner, thereby yielding consistent results. The advantages observed at low and medium threshold levels indicate notable improvements in segmentation quality and preservation of structural integrity. However, the performance gaps tend to diminish at higher threshold levels, suggesting that the hybrid algorithm exhibits stronger optimization power under limited threshold conditions. However, the primary metrics used in this study (PSNR, SSIM, FSIM, and NCC) assess pixel-level, structural, and feature fidelity between the original image and the segmentation output. Although these metrics demonstrate the algorithm's effectiveness in preserving image quality and structural consistency, they do not directly

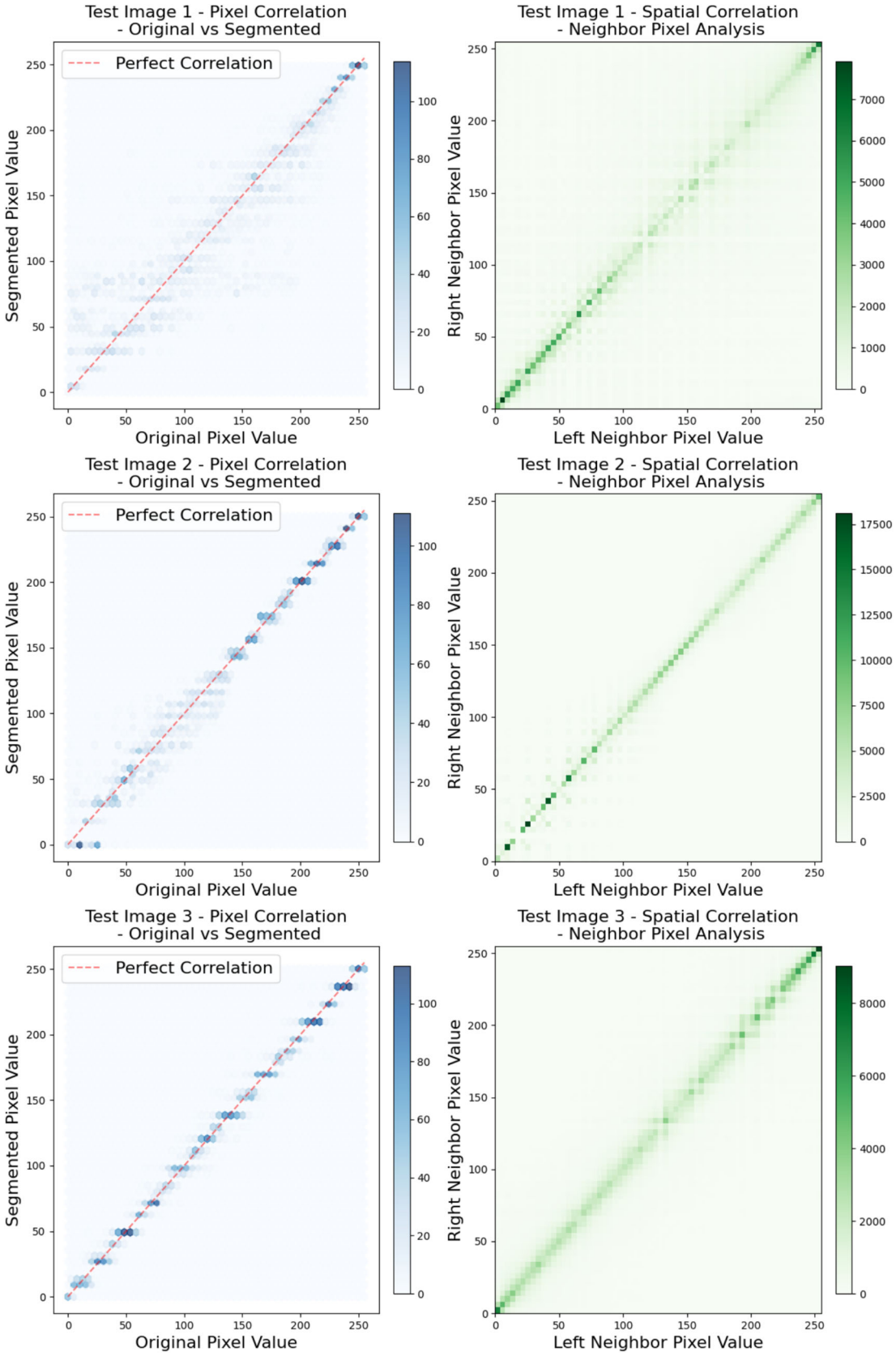

Fig. 7 Spatial correlation and neighbor pixel analysis on test images

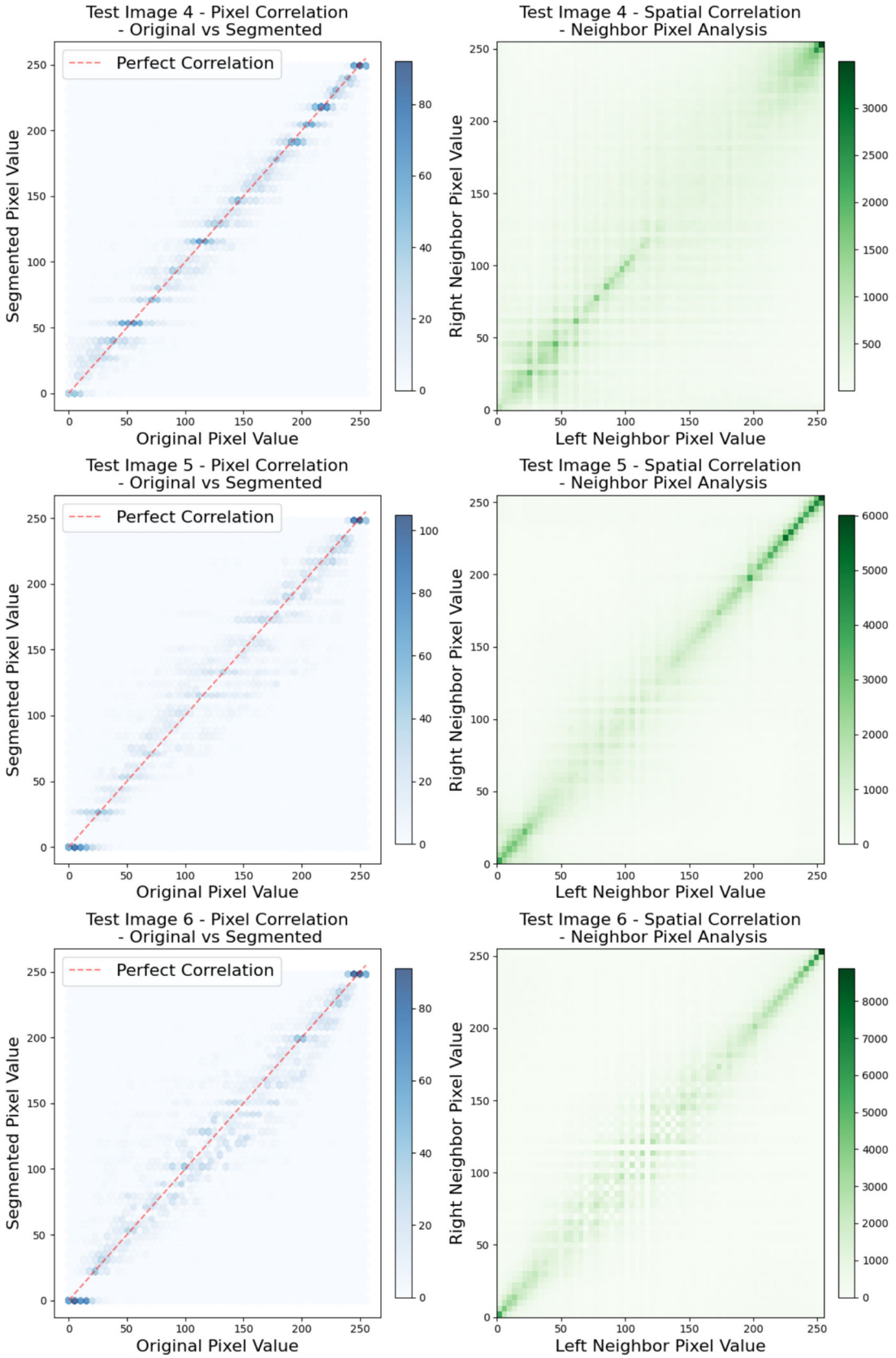

Fig. 7 continued

measure the accuracy of the segmentation task itself (i.e., the precision of assigning pixels to the correct classes) nor boundary accuracy (e.g., IoU). Therefore, for application-specific evaluations that require higher precision, the use of complementary metrics is recommended. Furthermore, the consistent outcomes in SSIM and NCC confirm the reliability of the proposed method in preserving the structural characteristics of images. The results obtained in this study indicate that the RSA–HGSO algorithm preserves overall image integrity to a high degree. Nevertheless, certain limitations inherent to the multi-level thresholding approach were also observed. First, the thresholding process reduces micro-contrast in fine textures, causing neighbor-pixel correlation to be lower than pixel-to-pixel correlation. This effect may lead to detail loss in applications where high-frequency patterns are critical. Additionally, banding and minor deviations appear at the extreme ends of the intensity distribution, which can exaggerate intra-class variance if class boundaries coincide with these ranges. The grid-like patterns observed in neighbor-pixel analyses indicate quantization artifacts arising from inter-level jumps and can introduce visual irregularities at low threshold numbers. Similarly, in high-texture scenes, scatter around the diagonal increases, reflecting the sensitivity of specific class thresholds to local optima. Finally, although global correlation coefficients exhibit high values, they may not always capture small but critical boundary errors in class labels. Therefore, for application-specific evaluations requiring higher precision, the use of supplementary metrics such as edge similarity or Intersection over Union (IoU) is recommended. On the other hand, factors such as parameter selection and data diversity should be considered, as they may influence the results. The absence of systematic evaluation of parameter configurations across different datasets or problem scenarios implies that the method's performance could be condition dependent. Therefore, parameter sensitivity analyses and experiments on large-scale datasets from diverse sources are expected to enhance the generalizability of the approach. The findings indicate that the RSA–HGSO algorithm is notable not only in terms of academic accuracy metrics but also with respect to image integrity preservation and practical applicability. High pixel-level correlation coefficients demonstrate that the algorithm largely preserves the original brightness ordering, while neighbor-pixel correlations reveal that local structural relationships remain substantially intact after segmentation. This capability supports reliable outcomes in time-critical scenarios, such as real-time image processing for disaster management and agricultural monitoring. Furthermore, the high PSNR and SSIM values observed at low-to-medium threshold levels indicate accurate delineation of class boundaries and macrostructures. The algorithm's computational efficiency and adaptive design facilitate its integration into practical application environments, including cloud-based geographic information systems (GIS) and mobile decision-support platforms, rendering it suitable for large-scale data analysis workflows.

6 Limitation

Despite its strengths, this study has certain limitations. First, the dataset is restricted to satellite images obtained from the NASA Visible Earth platform. This raises uncertainty regarding the algorithm's generalizability across different satellite types or sensor conditions. Second, in order to maintain lower computational complexity, an Otsu–Kapur hybrid-based fitness function was employed. Consequently, more advanced content-adaptive or deep learning–based objective functions were not considered. Additionally, as a limitation of the study, the algorithm's performance is evaluated primarily through image fidelity metrics (PSNR, SSIM, FSIM, and NCC). Although these metrics measure image quality, they do not directly assess classification accuracy (e.g., accuracy, IoU, or F1 score). This limitation restricts the ability to fully determine the method's absolute segmentation performance. This choice may have prevented the algorithm's flexibility and adaptability from being fully tested. Additionally, the parameter settings were determined experimentally, which could limit the applicability of the method to diverse scenarios. In real-time or large-scale data processing contexts, the current parameter configuration may be insufficient. Thus, strategies to reduce computational cost and automatic parameter optimization techniques will play a critical role in overcoming these limitations in future work. As the final limitation of this study, no systematic sensitivity analysis is conducted regarding the influence of the weighting coefficient α in the hybrid objective function on overall performance. This coefficient is fixed at 0.5 in the experimental evaluations. However, how variations toward $\alpha \rightarrow 1$ (Otsu-dominant) and $\alpha \rightarrow 0$ (Kapur-dominant) affect the results across different spectral or noisy contexts of satellite imagery has not been investigated. This omission limits the ability to fully determine the method's generalizability and its optimal balance. A comprehensive sensitivity analysis of the α coefficient will therefore constitute an important focus of future work.

7 Conclusion and future works

Multilevel segmentation of satellite imagery holds direct application potential in numerous critical domains, including disaster management, agricultural yield estimation, urban growth monitoring, and environmental change tracking. However, in high-resolution and structurally complex color satellite data, traditional methods face limitations in terms of

computational cost and accuracy, particularly as the number of thresholds increases. In this study, a novel hybrid metaheuristic approach, RSA–HGSO, is proposed for the multilevel image thresholding problem by adaptively integrating the Reptile Search Algorithm (RSA) with Henry Gas Solubility Optimization (HGSO). Unlike conventional hybrids that execute exploration and exploitation phases sequentially, the proposed adaptive framework dynamically distributes these processes to achieve a balanced search strategy. Experimental results demonstrate that RSA–HGSO provides particularly high accuracy at low and medium threshold levels. The algorithm achieves an average PSNR of 27.94 dB, SSIM of 0.9340, and FSIM of 0.9542, indicating higher structural similarity and visual quality compared to the benchmark methods. Nevertheless, the statistical analyses conducted (Wilcoxon test) indicate that the performance achieved by RSA–HGSO does not exhibit a statistically significant difference when compared with other competitive algorithms. This result confirms that the fundamental strength of the method lies in providing a statistically equivalent and balanced alternative to the performance of the individual algorithms. Correlation analyses further reveal that post-segmentation pixel-level Pearson $= 0.9557$ and Spearman $= 0.9549$ values preserve approximately 91% of the original intensity distribution, while neighbor-pixel analyses with Pearson $= 0.8042$ and Spearman $= 0.8051$ confirm that local structural integrity is largely maintained. These findings indicate that the algorithm reliably preserves both visual quality and structural coherence, supporting its practical applicability in real-world scenarios.

Nevertheless, several opportunities exist to broaden the scope of the method. Future research will focus on the following directions:

- Parameter Sensitivity Analysis: Systematic optimization of exploration–exploitation balance parameters for diverse satellite imaging conditions.
- Advanced Fitness Functions: Investigation of content-adaptive and deep learning–assisted objective functions in addition to traditional Otsu-based methods.
- Large-Scale Datasets: Cross-validation on datasets acquired from different satellite sensors and geographical regions.
- Post-Processing Modules: Integration of deep learning–based post-processing strategies to further enhance segmentation accuracy.
- Real-Time Applications: Validation of the algorithm's computational efficiency in mobile and real-time remote sensing systems. This could be further enhanced by incorporating dynamic split computing [47], which has the potential to optimize performance and reduce computational overhead in such applications.

Author contributions M.Faruk Şahin: Conceptualization, Methodology, Software, Validation, Formal analysis, Investigation, Data Curation, Visualization, Writing—Original Draft Ferzat Anka: Conceptualization, Methodology, Validation, Formal analysis, Investigation, Data Curation, Supervision, Writing—Original Draft.

Funding Open access funding provided by the Scientific and Technological Research Council of Türkiye (TÜBİTAK). No funding.

Data availability Available on request.

Declarations

Conflict of interest The authors declare no conflict of interest.

Consent for publication Not applicable. The data presented in this study are anonymized and do not contain identifiable information.

References

1. Jain, R., Bhu, H., Pandey, A.K., et al.: Base-metal exploration by using remote sensing, geological, geophysical, and geochemical datasets with clues from ancient mining: a comprehensive review on Aravalli-Delhi Fold Belt, Rajasthan, India. Adv. Space Res. **75**, 277–315 (2025). https://doi.org/10.1016/j.asr.2024.09.038
2. Zhang, J., Shao, Z., Ding, Q., et al.: AERNet: an attention-guided edge refinement network and a dataset for remote sensing building change detection. IEEE Trans. Geosci. Remote Sens. **61**, 1–16 (2023). https://doi.org/10.1109/TGRS.2023.3300533
3. Zhang, S., Ma, J., Zhang, X., et al.: Atmospheric remote sensing for anthropogenic methane emissions: applications and research opportunities. Sci. Total. Environ. **893**, 164701 (2023). https://doi.org/10.1016/j.scitotenv.2023.164701
4. Asadzadeh, S., Oliveira, W.J.D., Souza Filho, C.R.D.: UAV-based remote sensing for the petroleum industry and environmental monitoring: state-of-the-art and perspectives. J. Pet. Sci. Eng. **208**, 109633 (2022). https://doi.org/10.1016/j.petrol.2021.109633
5. Victor, N., Maddikunta, P.K.R., Mary, D.R.K., et al.: Remote sensing for agriculture in the era of Industry 5.0—a survey. IEEE J. Sel. Top. Appl. Earth Observ. Remote Sens. **17**, 5920–5945 (2024). https://doi.org/10.1109/JSTARS.2024.3370508
6. Yu, D., Fang, C.: Urban remote sensing with spatial big data: a review and renewed perspective of urban studies in recent decades. Remote Sens. **15**, 1307 (2023). https://doi.org/10.3390/rs15051307
7. Mohd Daud, S.M.S., Mohd Yusof, M.Y.P., Heo, C.C., et al.: Applications of drone in disaster management: a scoping review. Sci. Justice **62**, 30–42 (2022). https://doi.org/10.1016/j.scijus.2021.11.002

8. Wang, J., Zhen, J., Hu, W., et al.: Remote sensing of soil degradation: progress and perspective. Int. Soil Water Conserv. Res. **11**, 429–454 (2023). https://doi.org/10.1016/j.iswcr.2023.03.002
9. Al Deep, M., Araffa, S.A.S., Mansour, S.A., et al.: Geophysics and remote sensing applications for groundwater exploration in fractured basement: a case study from Abha area, Saudi Arabia. J. Afr. Earth Sci. **184**, 104368 (2021). https://doi.org/10.1016/j.jafrearsci.2021.104368
10. Feroz, S., Abu Dabous, S.: UAV-based remote sensing applications for bridge condition assessment. Remote Sensing **13**, 1809 (2021). https://doi.org/10.3390/rs13091809
11. Yang, Z., Yu, X., Dedman, S., et al.: UAV remote sensing applications in marine monitoring: knowledge visualization and review. Sci. Total. Environ. **838**, 155939 (2022). https://doi.org/10.1016/j.scitotenv.2022.155939
12. Aldoğan, C.F., Aksu, K., Demirel, H.: Enhancement of Sentinel-2A images for ship detection via Real-ESRGAN model. Appl. Sci. **14**, 11988 (2024). https://doi.org/10.3390/app142411988
13. Yao, L., Liu, T., Qin, J., et al.: Tree counting with high spatial-resolution satellite imagery based on deep neural networks. Ecol. Indic. **125**, 107591 (2021). https://doi.org/10.1016/j.ecolind.2021.107591
14. Akosah, S., Gratchev, I.: Systematic review of post-wildfire landslides. GeoHazards **6**, 12 (2025). https://doi.org/10.3390/geohazards6010012
15. Xu, H., Zhang, G., Zhou, Z., et al.: Development of a novel burned-area subpixel mapping (BASM) workflow for fire scar detection at subpixel level. Remote Sens. **14**, 3546 (2022). https://doi.org/10.3390/rs14153546
16. Yang, C., Wu, G., Ding, K., et al.: Improving land use/land cover classification by integrating pixel unmixing and decision tree methods. Remote Sens. **9**, 1222 (2017). https://doi.org/10.3390/rs9121222
17. Reis, L.G.D.M., Souza, W.D.O., Ribeiro Neto, A., et al.: Uncertainties involved in the use of thresholds for the detection of water bodies in multitemporal analysis from Landsat-8 and Sentinel-2 images. Sensors **21**, 7494 (2021). https://doi.org/10.3390/s21227494
18. Seyyedabbasi, A.: A hybrid multi-strategy optimization metaheuristic algorithm for multi-level thresholding color image segmentation. Appl. Sci. **15**, 7255 (2025). https://doi.org/10.3390/app15137255
19. Hu, P., Han, Y., Zhang, Z., et al.: A multi-level thresholding image segmentation algorithm based on equilibrium optimizer. Sci. Rep. **14**, 29728 (2024). https://doi.org/10.1038/s41598-024-81075-w
20. Wu, B., Zhu, L., Cao, J., et al.: A hybrid preaching optimization algorithm based on Kapur entropy for multilevel thresholding color image segmentation. Entropy **23**, 1599 (2021). https://doi.org/10.3390/e23121599
21. Houssein, E.H., Mohamed, G.M., Ibrahim, I.A., et al.: An efficient multilevel image thresholding method based on improved heap-based optimizer. Sci. Rep. **13**, 9094 (2023). https://doi.org/10.1038/s41598-023-36066-8
22. Chong, H.Y., Yap, H.J., Tan, S.C., et al.: Advances of metaheuristic algorithms in training neural networks for industrial applications. Soft. Comput. **25**, 11209–11233 (2021). https://doi.org/10.1007/s00500-021-05886-z
23. Şahin, M.F., Anka, F.: Metaheuristics role in image processing and computer vision applications: a comprehensive review. Clust. Comput. **28**, 871 (2025). https://doi.org/10.1007/s10586-025-05610-8
24. Giuliani, D.: Metaheuristic algorithms applied to color image segmentation on HSV space. J. Imaging **8**, 6 (2022). https://doi.org/10.3390/jimaging8010006
25. Brajević, I., Ignjatović, J.: Multilevel thresholding of color images using globally informed artificial bee colony algorithm. Sci. Rep. **15**, 22041 (2025). https://doi.org/10.1038/s41598-025-05238-z
26. Kurban, R., Durmus, A., Karakose, E.: A comparison of novel metaheuristic algorithms on color aerial image multilevel thresholding. Eng. Appl. Artif. Intell. **105**, 104410 (2021). https://doi.org/10.1016/j.engappai.2021.104410
27. Zhang, K., He, M., Dong, L., et al.: The application of Tsallis entropy based self-adaptive algorithm for multi-threshold image segmentation. Entropy **26**, 777 (2024). https://doi.org/10.3390/e26090777
28. Lei, S., Lu, M., Lin, J., et al.: Remote sensing image denoising based on improved semi-soft threshold. SIViP **15**, 73–81 (2021). https://doi.org/10.1007/s11760-020-01722-3
29. Tan, J., Tang, Y., Liu, B., et al.: A self-adaptive thresholding approach for automatic water extraction using Sentinel-1 SAR imagery based on OTSU algorithm and distance block. Remote Sens. **15**, 2690 (2023). https://doi.org/10.3390/rs15102690
30. Che, L., Li, S., Liu, X.: Improved surface water mapping using satellite remote sensing imagery based on optimization of the Otsu threshold and effective selection of remote-sensing water index. J. Hydrol. **654**, 132771 (2025). https://doi.org/10.1016/j.jhydrol.2025.132771
31. Ren, J., Wang, J., Chen, R., et al.: Remote sensing identification of shallow landslide based on improved otsu algorithm and multi feature threshold. Front. Earth Sci. **12**, 1473904 (2024). https://doi.org/10.3389/feart.2024.1473904
32. Wu, X., Wang, L., Wu, C., et al.: Semantic segmentation of remote sensing images using multiway fusion network. Signal Process. **215**, 109272 (2024). https://doi.org/10.1016/j.sigpro.2023.109272
33. Zhu, X., Zhang, Z., He, Y., et al.: LandslideNet: a landslide semantic segmentation network based on single-temporal optical remote sensing images. Adv. Space Res. **74**, 4616–4638 (2024). https://doi.org/10.1016/j.asr.2024.07.038
34. Nandhini, K., Porkodi, R.: A new fusion of mutual information and Otsu multilevel thresholding technique for hyperspectral band selection. Egypt. Inform. J. **22**, 133–143 (2021). https://doi.org/10.1016/j.eij.2020.06.002
35. Yu, J., Mao, P., Wu, W., et al.: TSNET: a solid waste instance segmentation model in China based on a Two-Step detection strategy and satellite remote sensing images. Int. J. Appl. Earth Obs. Geoinf. **136**, 104366 (2025). https://doi.org/10.1016/j.jag.2025.104366
36. Zhu, Q., Liao, C., Hu, H., et al.: MAP-Net: multiple attending path neural network for building footprint extraction from remote sensed imagery. IEEE Trans. Geosci. Remote Sens. **59**, 6169–6181 (2021). https://doi.org/10.1109/TGRS.2020.3026051
37. Rahaman, J., Sing, M.: An efficient multilevel thresholding based satellite image segmentation approach using a new adaptive cuckoo search algorithm. Expert Syst. Appl. **174**, 114633 (2021). https://doi.org/10.1016/j.eswa.2021.114633
38. Hosny, K.M., Khalid, A.M., Hamza, H.M., et al.: Multilevel thresholding satellite image segmentation using chaotic coronavirus optimization algorithm with hybrid fitness function. Neural Comput. Appl. **35**, 855–886 (2023). https://doi.org/10.1007/s00521-022-07718-z
39. Chaoxi, L., Lifang, H., Songwei, H., et al.: An improved bald eagle algorithm based on Tent map and Levy flight for color satellite image segmentation. Signal Image Video Process. **17**, 2005–2013 (2023). https://doi.org/10.1007/s11760-022-02413-x
40. Pal, R., Mukhopadhyay, S., Chakraborty, D., et al.: Very high-resolution satellite image segmentation using variable-length multi-objective genetic clustering for multi-class change detection. J. King Saud Univ. - Comput. Inf. Sci. **34**, 9964–9976 (2022). https://doi.org/10.1016/j.jksuci.2021.12.023
41. Snehlata, M.N., Gelbukh, A.: Change Detection in Remote-Sensed Data by Particle Swarm Optimized Edge Detection Image Segmentation Technique. In: Raj, J.S., Iliyasu, A.M., Bestak, R., et al. (eds.) Innov Data Commun Technol Appl, vol. 59, pp. 809–817.

Springer Singaporep, Singapore (2021). https://doi.org/10.1007/978-981-15-9651-3_65
42. Kurban, T.: Region based multi-spectral fusion method for remote sensing images using differential search algorithm and IHS transform. Expert Syst. Appl. **189**, 116135 (2022). https://doi.org/10.1016/j.eswa.2021.116135
43. Fan, F., Liu, G., Geng, J., et al.: Optimization of remote sensing image segmentation by a customized parallel sine cosine algorithm based on the Taguchi method. Remote Sens. **14**, 4875 (2022). https://doi.org/10.3390/rs14194875
44. Fu J, Setthawong R. A Modified Snake Optimizer Algorithm with Otsu-based Method for Satellite Image Segmentation. Proc. 13th Int. Conf. Adv. Inf. Technol., Bangkok Thailand: ACM; 2023, p. 1–7. https://doi.org/10.1145/3628454.3631198.
45. Jia, H., Lang, C., Oliva, D., et al.: Dynamic harris hawks optimization with mutation mechanism for satellite image segmentation. Remote Sens. **11**, 1421 (2019). https://doi.org/10.3390/rs11121421
46. NASA Visible Earth n.d. https://visibleearth.nasa.gov/.
47. Sahin, M.F., Yeganli, S.F., Kiani, F.: DSPCI-MTL: Dynamic split point computing in multi-task learning implementation with collaborative intelligence. Alex. Eng. J. **124**, 404–421 (2025). https://doi.org/10.1016/j.aej.2025.03.115

M. Faruk Şahin received his bachelor's degree in Electrical and Electronics Engineering from Istanbul Gelişim University in 2020. He completed his master's degree in Computer Engineering at Fatih Sultan Mehmet Vakıf University and is currently pursuing a Ph.D. in Computer Engineering at National Defence University. His primary research areas include artificial intelligence, digital image processing, biotechnology, and the internet of things (IoT). He has several research articles in SCI journals in these fields and currently works as a research assistant at Istanbul Atlas University.

Ferzat Anka received his bachelor's and master's degrees in Computer Software Engineering from Azad University in 2006 and 2009, respectively. He completed his Ph.D. in computer engineering at Dokuz Eylül University, Türkiye, in 2014. Prof. Anka has extensive academic and industrial experience, both nationally and internationally. He has founded and led research laboratories in wireless sensor networks (WSN), internet of things (IoT), and machine learning (ML). His research interests include WSNs, smart cities, IoT, artificial intelligence, and optimization algorithms. He has published more than 50 research articles in SCI journals and has three published books. Prof. Anka is currently a professor in the department of computer engineering at Fatih Sultan Mehmet Vakif University, Istanbul, Turkey. He is a member of several professional societies, including the TÜBİTAK young research group and KOSGEB.